Amelioration of Brain Histone Methylopathies by Balancing a Writer-Eraser Duo KMT2A-KDM5C

Christina N. Vallianatos[1, 2], Brynne Raines[3], Robert S. Porter[1,2], Katherine M. Bonefas[1,4], Michael C. Wu[5], Patricia M. Garay[1,4], Katie M. Collette[3], Young Ah Seo[6], Yali Dou[7], Catherine E. Keegan[1,8], Natalie C. Tronson[3,*], and Shigeki Iwase[1,*]

[1]Department of Human Genetics, Michigan Medicine, University of Michigan, Ann Arbor, MI 48109

[2]Genetics and Genomics Graduate Program, University of Michigan, Ann Arbor, MI 48109

[3]Department of Psychology, College of LS&A, University of Michigan, Ann Arbor, MI 48109

[4]The University of Michigan Neuroscience Graduate Program

[5]Neurodigitech, LLC, San Diego, CA

[6]Department of Nutritional Sciences, School of Public Health, University of Michigan, Ann Arbor, MI 48109

[7]Department of Pathology, Michigan Medicine, University of Michigan, Ann Arbor, MI 48109

[8]Department of Pediatrics, Michigan Medicine, University of Michigan, Ann Arbor, MI 48109

*Co-corresponding authors

Please address correspondence to: siwase@umich.edu and ntronson@umich.edu

Abstract

Histone H3 lysine 4 methylation (H3K4me) is extensively regulated by seven writer and six eraser enzymes in mammals. Nine H3K4me enzymes are associated with neurodevelopmental disorders to date, indicating their important roles in the brain. Opposing activities of writer-eraser enzymes highlight activity modulation as a therapeutic strategy. However, interplay among H3K4me enzymes in the brain remains largely unknown. Here, we show functional interactions of a writer-eraser duo, *KMT2A* and *KDM5C*, which are responsible for Wiedemann-Steiner Syndrome (WDSTS), and mental retardation X-linked syndromic Claes-Jensen type (MRXSCJ), respectively. Despite opposite enzymatic activities, the WDSTS and MRXSCJ mouse models, deficient for either *Kmt2a* or *Kdm5c*, shared reduced dendritic spines and increased aggression. Double mutation of *Kmt2a* and *Kdm5c* clearly reversed dendritic morphology deficits and key behavioral traits including aggression, and partially corrected altered transcriptomes and H3K4me landscapes. Thus, our study uncovers common yet mutually suppressive aspects of the WDSTS and MRXSCJ models and provides a proof of principle for balancing a single writer-eraser pair to ameliorate their associated disorders.

Introduction

Dysregulation of histone methylation has emerged as a major contributor to neurodevelopmental disorders (NDDs) such as autism spectrum disorders and intellectual disabilities (1-3). Histone methylation can be placed on a subset of lysines and arginines by histone methyltransferases (writer enzymes) and serves as a signaling platform for a variety of nuclear events including transcription (4). Reader proteins specifically recognize methylated histones, thereby converting methylation signals into higher-order chromatin structures (5). Histone methylation can be removed by a set of histone demethylases (eraser enzymes) (6). Pathogenic variants in all three classes of methyl-histone regulators cause NDDs, indicating critical, yet poorly understood roles of histone methylation dynamics in brain development and function (7-9).

Histone H3 lysine 4 methylation (H3K4me) is one of the most well-characterized histone modifications. H3K4me is primarily found at transcriptionally active areas of the genome. The three states, mono-, di-, and tri-methylation (H3K4me1-3), uniquely mark gene regulatory elements and play pivotal roles in distinct steps of transcription. While H3K4me3/2 are enriched at transcriptionally engaged promoters, H3K4me1 is a hallmark of transcriptional enhancers (10, 11). At promoters, H3K4me3 contributes to recruitment of general transcription machinery TFIID and RNA polymerase II (12, 13). H3K4me1 has been shown to tether BAF, an ATP-dependent chromatin remodeling complex, to enhancers (14).

H3K4me is extensively regulated by seven methyltransferases and six demethylases in mammals (6). Consistent with the important roles of H3K4me in transcriptional regulation, genomic distribution of H3K4me appears highly dynamic during brain development (15), in which widespread gene expression changes take place. Developmental H3K4me dynamics appear to be altered in the prefrontal cortices of individuals with autism (16, 17). However, the contributions of each of the 13 enzymes in the dynamic H3K4me landscapes of the developing brain remain largely unknown. Strikingly, genetic alterations in nine of the 13 H3K4me enzymes and at least two H3K4me readers have been associated with human NDDs to date, indicating the critical roles of H3K4me balance (18) (Figure 1A). These human conditions can be collectively referred to as brain H3K4 methylopathies and point to non-redundant yet poorly understood roles of these genes controlling this single post-translational modification for faithful brain development.

As histone modifications are reversible, one can, in theory, correct an imbalance by modulating the writers or erasers. Chemical inhibitors of histone deacetylases (HDACs) have been successfully used to rescue phenotypes in mouse models of NDDs. HDAC inhibitors were able to ameliorate learning disabilities in mouse models of Rubinstein-Taybi and Kabuki syndromes, which are deficient for CREBBP or KMT2D, writer enzymes for histone acetylation or H3K4me, respectively (19, 20). However, none of these chemical compounds has yet been proven applicable to human NDDs. Moreover, the HDAC inhibitors, such as SAHA and AR-42, used in these studies interfere with multiple HDACs (21), which could potentially result in widespread side effects. Given

the non-redundant roles of the H3K4me enzymes, a more specific perturbation is desirable.

In order to achieve specific modulation of H3K4me rather than inhibiting multiple histone modifiers in a given NDD, an important first step is to delineate functional relationships between the H3K4 enzymes. In the present work, we focus on a pair of NDD-associated writer/eraser enzymes: KMT2A and KDM5C. Haploinsufficiency of *KMT2A* underlies Weidemann-Steiner Syndrome (WDSTS), characterized by developmental delay, intellectual disability, characteristic facial features, short stature, and hypotonia (22, 23). Loss of KDM5C function defines Mental Retardation, X-linked, syndromic, Claes Jensen type (MRXSCJ), in which individuals display an intellectual disability syndrome with aggression, short stature, and occasional autism comorbidity (24-27). Mouse models have provided experimental support for causative impacts of KMT2A and KDM5C deficiencies in impaired cognitive development. Heterozygous *Kmt2a* knockout (KO) mice show compromised fear learning (28), and excitatory-neuron-specific *Kmt2a* deletion similarly led to impaired learning, memory, and anxiety behaviors, as well as altered H3K4me3 distributions and transcriptomes (29, 30). In these studies, however, the social behavior and relevant cellular consequences of *Kmt2a* loss were not examined. *Kdm5c*-knockout (KO) mice mimic many MRXSCJ features, including small body size, aggressive behavior, and reduced social activity and learning (31, 32). *Kdm5c*-KO neurons in the basolateral amygdala exhibit malformation of dendritic arbors and spines along with misregulation of neurodevelopmental genes. However, the functional relationships between KMT2A and KDM5C, e.g. how deficiencies in opposing

enzymatic activities can lead to same learning deficits, remain elusive. Additionally, despite the strong association with NDDs, successful modulation of histone methylation to restore normal brain physiology has not been reported in these or any other animal models of histone methylopathies.

In the present work, we tested whether modulating either single H3K4me writer or eraser can ameliorate the neurodevelopmental symptoms observed in the WDSTS and MRXSCJ mouse models. We generated *Kmt2a*-, *Kdm5c*-double mutant (DM) mice, and performed systematic comparisons between wild-type (WT), single mutants, and DM mice.

Results

KMT2A and KDM5C co-exist broadly in the brain

We first examined expression patterns of KMT2A and KDM5C using publicly available resources, and found the two genes are broadly expressed throughout brain regions of adult mice and humans (Figure S1) (33-37) (38). *Kmt2a* and *Kdm5c* are expressed at comparable levels in all major excitatory and inhibitory neuron subtypes as well as glia cells in mouse visual cortices (Figure S1A), and also throughout mouse brains (Figure S1B). Consistently, developing and aging human brains express *KMT2A* and *KDM5C* at high, steady levels (Figure S1C). Thus, both writer and eraser are co-expressed across brain cell types, regions, and developmental stages in both humans and mice.

Generation of *Kmt2a-Kdm5c* double-mutant (DM) mice

To test genetic interaction of *Kmt2a* and *Kdm5c*, we generated *Kmt2a-Kdm5c* double-mutant (DM) mice. Experimental mice were F1 hybrids of the two fully congenic laboratory mouse strains: 129S1/SvImJ *Kmt2a*$^{+/-}$ males (39) and C57BL/6J *Kdm5c*$^{+/-}$ females (31) (Figure 1B). This cross resulted in the following genotypes of male mice in an identical genetic background: wildtype (WT); *Kmt2a* heterozygote (*Kmt2a*-HET: *Kmt2a*$^{+/-}$), *Kdm5c* hemizygous knock-out (*Kdm5c*-KO: *Kdm5c*$^{-/y}$), and *Kmt2a-Kdm5c* double-mutant (DM: *Kmt2a*$^{+/-}$, *Kdm5c*$^{-/y}$), thereby allowing us to perform a systematic comparison between the WDSTS model (*Kmt2a*-HET), the MRXSCJ model (*Kdm5c*-KO), and their composite (DM). We focus on males, because MRXSCJ predominantly

affects males and *Kdm5c*-heterozygous female mice exhibit only minor cognitive deficits (32).

These mice were born at expected Mendelian ratios of 25% per genotype, demonstrating the DM mice were not synthetic lethal (Figure 1C). Genotypes were confirmed at RNA and DNA levels (Figure S2A-C), and protein level for KDM5C (Figure S2D). Brain anatomy showed no gross deformities in any of the genotypes (Figure S2E). Body weight, during the course of development and in adult, however, was reduced in the two single mutants as well as in DM mice (Figure 1D, Figure S2F). Note that for all the four-way comparisons in this study, we first represent the *p*-values from one-way ANOVA tests of genotype-phenotype interaction with histograms of measured values. We then report *p*-values from post-hoc tests of all six genotype comparisons with 95% confidence intervals of group mean differences. Both *Kmt2a*-Het and *Kdm5c*-KO mice showed significant body weight reduction compared to WT (Figure 1D, One Way ANOVA: $F(3, 55) = 10.28$, $p < 1.0 \times 10^{-4}$, Tukey's multiple comparison test: WT vs 2A: $p = 0.008$, WT vs 5C: $p = 0.008$). DM body weight was significantly smaller compared to WT (DM vs WT: $p < 1.0 \times 10^{-4}$). Thus, loss of *Kdm5c* and *Kmt2a* heterozygosity both led to growth retardation, which was not corrected but rather slightly exacerbated in DM mice.

Memory impairments in *Kdm5c*-KO were ameliorated in DM

We first sought to determine the effect of loss of *Kmt2a* and/or *Kdm5c* on mouse behavior through a battery of behavioral tests. Learning and memory measured by two

independent tests, contextual fear conditioning (CFC) and novel object recognition (NOR), significantly interacted with genotypes (CFC: F (3,64) = 2.83, p = 0.046). NOR: F(3,64) = 3.20, p = 0.030). In accordance with previous findings (31, 32), *Kdm5c*-KO showed significant deficits in associative fear memory in the CFC (Figure 2A, WT vs 5C: p = 0.018, WT vs 2A: p = 0.789). In the NOR, where WT mice showed preference for the new object, *Kdm5c*-KO mice tended to avoid the novel object (Figure 2B) (WT vs 5C: p = 0.007). Previous work reported that homozygous deletion of *Kmt2a* in excitatory hippocampal neurons leads to impaired fear memory in the CFC (30). In our tests, *Kmt2a*-HET mice showed no deficits in either CFC or NOR (Figure 2A-B) (CFC: p = 0.789; NOR; p = 0.888), indicating that *Kmt2a*-heterozygosity does not lead to learning impairment measured in these assays. Importantly, DM mice also showed no differences from WT mice (Figure 2A-B) (CFC: p = 0.246; NOR: p = 0.756), suggesting that *Kmt2a* heterozygosity rescues memory deficits of *Kdm5c*-KO mice. These differences in memory tasks were not attributable to differences in locomotor activity or shock responsiveness, as none of these parameters showed significant differences among the genotypes (Figure 2C-D).

Social behavior in the single and double mutants

We next examined social behavior using the three independent behavioral paradigms. First, social interaction was tested with the three-chambered preference test. *Kmt2a*-HET mice showed no differences from WT (Figure 3A, WT vs 2A: p = 0.082) in accordance with previous tests in conditional *Kmt2a*-KO mice (30). In contrast, *Kdm5c*-KO mice, as previously shown (31), exhibited significantly less preference for the

stranger mouse compared with WT animals (WT vs 5C: p= 0.002). Similar to *Kdm5c*-KO, DM mice spent less time with stranger mice compared to WT (WT vs DM: p = 0.011). No difference was detected between *Kdm5c*-KO and DM (5C vs DM: p= 0.709). These data indicate that *Kmt2a* heterozygosity does not alter social preference or rescue the deficit of *Kdm5c*-KO.

In tests of social dominance (Figure 3B), both *Kmt2a*-HET and *Kdm5c*-KO mice won more frequently against WTs (2A vs WT: 60.9%, p = 0.091, 5C vs WT: 68.4%, p = 0.008). In contrast, DM animals lost more than 80% of their bouts against WT (DM vs WT: $p = 1.47 \times 10^{-5}$). Although DM mice were slightly smaller compared to single mutants (Figure 1D), this is unlikely to drive submissive behaviors, as body mass has been shown to have minimal impact on social hierarchy unless excess difference (> 30%) is present between animals (40-42), which is not the case in our study (Figure 1D) (2A vs WT:11%, 5C vs WT: 17%, DM vs WT: 25%). These results indicate that the two single mutants share heightened social dominance and the double mutation reverses the social dominance.

Lastly, in the resident-intruder test, similar to other behavioral paradigms, overall effects of genotype were evident in both aggressive and submissive behavior (Figure 3C, aggressive behavior: $F(3,61) = 4.071$, p = 0.011, submissive behavior: ($F(3,61) = 4.071$, p = 0.011). The genotype effect on aggressive behaviors inversely correlated with that of submissive behavior, reinforcing the changes in specific behaviors rather than general locomotor activity. Both *Kmt2a*-HET and *Kdm5c*-KO show a trend of increased

aggression and decreased submission when we combine frequency of all aggressive or submissive behavior types compared to WT (Figure 3C). With regard to specific aggressive behavior, we found significantly increased darting (Figure S3A) in both *Kdm5c*-KO (p = 0.006) and *Kmt2a*-HET (p = 0.032) mice.

DM mice showed significantly reduced overall aggression compared to the two single mutants (Fig. 3C, DM vs 5C: p = 0.015, DM vs 2A: p = 0.011). Reciprocally, DM mice were more submissive compared to single mutants (DM vs 5C: p = 0.001, DM vs 2A: p = 0.011). Comparison between DM and WT mice did not yield any significant differences. However, DM mice showed a strong trend of greater submission compared to WT (aggression: DM vs WT: p = 0.189; submission: DM vs WT: p = 0.054); these findings are consistent with the results of the social dominance test described above. The decreased aggression and increased submission of DM relative to the single mutants were also observed in multiple behavior types, including mounting, chasing for aggression (Figure S3A) and cowering and running away for submission (Figures S3B). Thus, these results suggest that double mutations alleviate aggressive behavior of both *Kmt2a*-HET and *Kdm5c*-KO mice.

Together, the behavioral studies revealed more pronounced deficits in *Kdm5c*-KO animals compared to *Kmt2a*-HET mice in terms of memory and social interaction, while *Kmt2a*-HET and *Kdm5c*-KO mice shared increased social dominance and aggression. The consequences of double mutations varied between the tests, with clear rescue effects on cognitive tasks, dominant behavior, and aggression, and no effect on social

interactions. No behavioral traits were exacerbated in DM. Interestingly, DM mice showed opposite phenotypes in social dominance and aggression compared to single mutants, which is reminiscent of the increased spine density in the DM basolateral amygdala but not in the hippocampal CA1 (Figure 4). These results establish common and unique behavioral deficits of *Kdm5c*-KO and *Kmt2a*-HET mice and mutual suppression between the two genes in some of the behavioral traits.

Roles of KMT2A, KDM5C, and their interplay in neuronal morphology

Altered dendrite morphology is a hallmark of many human NDDs, as well as animal models of NDDs (31, 43-46). We previously found reduced dendritic length and spine density in basolateral amygdala (BLA) neurons of *Kdm5c*-KO adult male mice (31). Assessment of dendritic morphology in *Kmt2a*-HET has not been reported. We first performed comparative dendrite morphometry of pyramidal neurons in the BLA using Golgi staining for the four genotypes (Figure 4). For *Kdm5c*-KO neurons, we recapitulated our previous findings of reduced dendrite lengths (Figure 4A and B, one-way ANOVA followed by Tukey's multiple comparison test, WT vs 5C: $p = 0.034$) and lower spine density (Figure 4A and C, WT vs 5C: $p = 0.008$). Similar to *Kdm5c*-KO neurons, *Kmt2a*-HET cells exhibited a reduction in spine density (Figure 4B and C, WT vs 2A: $p = 0.005$) but not in dendritic length (WT vs 2A: $p = 0.177$).

Dendrite lengths of DM did not differ significantly from WT (Figure 4B, WT vs. DM: $p = 0.550$); however, these lengths were also not different from *Kdm5c*-KO (*Kdm5c*-KO vs. DM: $p = 0.534$), representing a weak restorative effect. In contrast, dendritic spine

density of DM showed a significant increase that surpassed a rescue effect: DM spine density was significantly higher than those of the other three genotypes (Figure 4C). As morphology of dendritic spines progressively changes during synaptogenesis and development (47) (Figure S4), we also asked whether developmental subtypes of dendritic spines were altered in any genotype. We did not find dramatic changes in spine morphology among the four genotypes (Figure 4D), indicating selective requirement of *Kdm5c* and *Kmt2a* for regulation of spine numbers.

Next we tested the impact of single and double mutations on morphology of hippocampal neurons (Fig. 4E and 4F). Since the ventral hippocampus CA1 (vCA1) receives inputs from BLA (48), we performed morphometry analyses of pyramidal neurons in this region. Genotype had significant impact on dendritic spine density (one-way ANOVA, F (3, 92) 11.51, $p < 1.0 \times 10^{-4}$) but not on dendritic length (F (3, 92) = 0.564, p=0.639). While dendritic length did not show any difference in *Kdm5c*-KO and *Kmt2a*-HET neurons, spine density was concomitantly decreased in the two single mutants compared to WT (WT vs 2A: $p = 2.0 \times 10^{-4}$, WT vs 5C: $p < 1.0 \times 10^{-4}$). In DM vCA1, spine density showed a trend of degrease compared to WT, yet this did not reach statistical significance (WT vs DM: $p = 0.066$). DM spine density was significantly higher than *Kdm5c*-KO (DM vs 5C: $p = 0.021$) but not compared to *Kmt2a*-HET (DM vs 2A: p=0.223). These analyses indicate reduced spine density in both *Kdm5c*-KO and *Kmt2a*-HET vCA1 neurons and its partial correction in DM.

Overall, we conclude that *Kmt2a*-HET and *Kdm5c*-KO share a reduced spine density in both BLA and vCA1. Double mutations led to reversal of spine phenotype in BLA and partial restoration of normal spine density in vCA1, supporting mutually suppressive roles of KMT2A and KDM5C in dendritic spine development.

Roles of KMT2A and KDM5C in mRNA expression

We previously showed *Kdm5c*-KO mice exhibit aberrant gene expression patterns in the amygdala and frontal cortex (31), and hippocampus (32). Excitatory-neuron specific conditional *Kmt2a*-KO mice were also characterized with altered transcriptomes in the hippocampus and cortex (29, 30). However, the global gene expression of *Kmt2a*-HET, which is akin to the WDSTS syndrome genotypes, has not been determined. To compare the impact of *Kmt2a*-heterozygosity and *Kdm5c*-KO on the transcriptomes, we performed mRNA-seq (49) using the amygdala and the hippocampus of adult mice with four animals per genotype. We confirmed the lack or reduction of reads from *Kdm5c* exons 11 and 12 and *Kmt2a* exons 8 and 9 in the corresponding mutants (Figure S2A-B). The accurate microdissection of brain regions was confirmed by stronger co-clustering of our data with another published mRNA-seq dataset from amygdala and hippocampus tissues (50) (Figure S5A). Principal component analysis (PCA) indicated that transcriptomic divergence was much larger between brain regions compared to the four genotypes (Figure S6A)

In the amygdala, we identified 132 differentially expressed genes (DEGs, *padj* < 0.1) in *Kdm5c*-KO (5C-DEGs) and no 2A-DEG (Figure 5A and S6). The hippocampus yielded a

consistently higher number of DEGs across the genotypes (344 5C-DEGs and 4 2A-DEGs). The small number of 2A-DEGs is likely due to the one remaining copy of *Kmt2a*. Given the increased social dominance (Figure 3B) and clear reduction of dendritic spines (Figure 4) in *Kmt2a*-HET mice, we reasoned that such phenotypes might be associated with mild gene misregulation, which was not detected by DEseq2. To be able to analyze the gene expression in *Kmt2a*-HET, we set a relaxed cut off ($p < 0.005$) and retrieved 78 and 139 genes as 2A-DEG from the amygdala and hippocampus, respectively (Figure 5B and S6). Table S1 lists all DEGs found in the study.

Between the amygdala and hippocampus, 5C-DEGs overlap substantially (72 DEGs, Figure S7A). The heat map analysis of DEG points to a similarity in dysregulation of not only 5C-DEGs but also 2A-DEGs between the two brain regions, which was not detected as identity of genes (Figure S7B). These data suggest that the two brain regions share gene expression programs that require KMT2A or KDM5C for their normal expression.

We first sought to compare the gene expression profiles between the single mutants. The majority of 5C-DEGs were upregulated and 2A-DEGs were downregulated (Figure 5A and 5B, S6). This result agrees with KMT2A's primary role as a transcriptional coactivator by placing H3K4me (39, 51, 52) and KDM5C's suppressive activity on transcription by removing this mark (53), yet KDM5C can also act as a positive regulator of transcription (54, 55). If KMT2A and KDM5C counteract, DEGs would be oppositely misregulated between the single mutants. Indeed, we found that 28-29% of 5C-DEGs

show signs of upregulation in *Kmt2a*-HET, while 8-17% of 2A-DEGs tend to be downregulated in *Kdm5c*-KO brain tissues (Figure S8A and S8B). While these minor fractions of DEGs show opposite changes between the single mutants, substantial fractions of DEGs were misregulated in the same directions (Figure S8A and S8B), which might be due to indirect consequences of gene manipulations. The same-direction changes reflect on the similar phenotypes observed in some of behavioral tests, including social dominance, and reduced spine density in the two single mutants (Figure 3 and 4).

Impact of double mutations on mRNA expression

If the double mutations fully restore the normal transcriptome, the DM transcriptome should resemble to that of WT over single mutants. However, the DM brain tissues had a similar number of DEGs as *Kdm5c*-KO (Figure 5A). Many DM-DEGs overlap with 5C-DEGs (84 in the amygdala and 116 in the hippocampus), and 30 DM-DEGs overlap with 2A-DEGs in the hippocampus (Figure S8C). Thus, the DM transcriptome still retains some mRNA misregulations of single mutants and does not fully return to the normal state, which may not be surprising given that only one of six writer or eraser enzymes was manipulated (Figure 1).

Next, we sought to test more quantitatively whether the transcriptome alterations in single mutants were restored in DM to some extent. We first compared fold changes of single-mutant DEGs as a group in DM. Expression of 5C-up-regulated genes was significantly lower in the DM amygdala and hippocampus (Paired Wilcoxon signed-rank

test, $p < 1.41 \times 10^{-8}$, Figure 5C). Reciprocally, expression of 2A-down-regulated genes was significantly higher in DM brain tissues ($p < 1.26 \times 10^{-8}$, Figure 5C). We then examined how individual DEGs behaved in DM. The fold changes of 5C-DEGs and 2A-DEGs in single mutants clearly correlated with those in DM, indicating that single-mutant DEGs are similarly dysregulated in DM in general. However, the slopes of linear regression were lower than 1 with statistical significance, suggesting the partial rescue effect (Figure 5D). The mildest rescue effect was observed in 5C-DEGs in the DM amygdala (linear regression slope=0.91±0.03), while 5C-DEGs in the hippocampus and 2A-DEGs-R exhibit more pronounced rescue effects (slope: 0.51~0.73). These results indicate that misregulation of genes in both *Kdm5c*-KO or *Kmt2a*-HET was partially corrected in the DM brain tissues.

We then sought to isolate genes that might have contributed to the rescue effects at cellular and behavioral levels. As shown by the red circles in Figure 5D, some DEGs exhibit stronger rescue effects than others. We selected these genes as potential drivers of rescue effects (see Materials & Methods). While 10 genes in the amygdala and 81 genes in the hippocampus drove rescue effects of 5C-DEGs, 36 genes in the amygdala and 46 genes in the hippocampus contributed to the partial restoration of normal 2A-DEGs expression in DM (Table S2). We then performed pathway analysis on these rescue-driving genes using the Enrichr program (56, 57). While 2A-rescue genes did not yield any statistically significant enrichment (*padj* < 0.05), 5C-rescued genes showed strong enrichment of a mouse KEGG pathway, “neuroactive ligand-receptor interaction” (*padj* = 5.60×10^{-3}, Odds ratio: 6.01). The following 10 genes contributed to

the enrichment: *Pomc*, *Adcy2*, *Agt*, *Adora2a*, *Mc3r*, *Gabre*, *P2ry14*, *Tacr1*, *Trh*, *and Lhb*. Except for *P2ry14*, all these genes have known roles in learning and memory or aggression (Table 1).

Interestingly, most of these genes encode peptide hormones, their receptors, or downstream signaling molecules. For example, Pro-opiomelanocortin (POMC) is a peptide hormone primarily known for its roles in regulating hypothalamic functions, such as feeding (58). In addition to its high expression in the hypothalamus, *Pomc* is also expressed in the amygdala and the hippocampus (58, 59). POMC signaling in these regions has been implicated in the cognitive decline of Alzheimer's disease as well as in drug-induced stress response (60, 61). Another gene in the list, *Mc3r*, encodes a POMC receptor. *Mc3r* is expressed in the hypothalamus and limbic structures such as the amygdala and hippocampus (62). Similar to *Pomc*, *Mc3r*'s roles have been primarily studied in the hypothalamus (63), yet this gene has also been implicated in hippocampal memory consolidation (64). Collectively, these results raise the possibility that aberrant peptide hormone signaling and its normalization underlie phenotypic outcomes of *Kdm5c*-KO and DM mice.

H3K4me3 landscapes in WDSTS and MRXSCJ models

H3K4me3 is a reaction product of KMT2A-mediated methylation (51), while a substrate for KDM5C-mediated demethylation (53, 65). We sought to determine the impact of KMT2A- and KDM5C-deficiencies and double mutation on the H3K4me3 landscape within the amygdala. In Western blot analyses, global H3K4me1-3 levels were not

altered dramatically in any mutant (Figure 6A). We thus performed H3K4me3 chromatin immunoprecipitation coupled with deep sequencing (ChIP-seq) to probe local changes genome-wide. To assess the IP specificity, we spiked-in an array of recombinant nucleosomes carrying 15 common methylations along with DNA barcodes appended to the Widom601 nucleosome positioning sequence (66) (see Methods). The two H3K4me3 nucleosomes dominated the Widom601-containing DNA in all IP reactions with negligible signals from other methylation states such as H3K4me1 or H3K4me2 (Figure S9A), demonstrating a superb specificity of the ChIP.

PCA analyses of H3K4me3 distribution indicated that WT and *Kmt2a*-HET are close each other, while *Kdm5c*-KO and DM cluster separately from the WT-2a-HET cluster. Reminiscent of the transcriptome data (Figure 5), we did not recover any differentially methylated regions (DMRs) in *Kmt2a*-HET, while *Kdm5c*-KO had 1,147 hypermethylated regions (Figure 6C, S9, padj < 0.05 in DEseq2, see method). In *Kdm5c*-KO, 583 loci are hypomethylated compared to WT, and these regions are highly methylated regions at baseline (Figure 6C and S9C). By relaxing the threshold, we obtained weak 2A-HET DMRs (Figure 6C, 357 hypermethylated and 240 hypomethylated). We then examined how these single-mutant DMRs behaved in the other single mutant. Compared to the transcriptome data (Figure S8A and S8B), we were able to recover more DMRs that are misregulated in opposite directions between the single mutants (Figure 6D). These results suggest that, as a primary substrate of the two enzymes, H3K4me3 changes represent the action of KMT2A and KDM5C more directly compared to mRNA expression. Comparable numbers of DMRs still show

same-direction H3K4me3 changes, which may again reflect indirect consequences of *Kmt2a* heterozygosity and *Kdm5c* deficiency.

Rescue effect of H3K4me3 landscapes in DM

We next examined the impact of double mutations on H3K4me3 distributions. Notably, in the PCA plot, the second replicate of DM was distant from the other two replicates and clustered closer with the WT-2A group, indicating that expressivity of rescue effect varies among individual animals (Figure 6B). The number of DMRs in DM are smaller than those of single mutants (Figure 6C). We then assessed how single-mutant DMRs behave in DM. Note that, we focus on hypomethylated loci in *Kmt2a*-HET and hypermethylated loci in *Kdm5c*-KO (colored loci in Figure 6D) based on the enzymatic activity of KMT2A and KDM5C. The opposite-direction 2A-DMRs showed complete normalization in DM, while the same-direction 2A-DMRs were even more hypomethylated in DM (Figure 6E). Likewise, the opposite-direction 5C-DMRs showed more pronounced rescue effect in DM compared to same-direction 5C-DMRs (Figure 6E). This direction-dependent rescue effect persisted even when we omitted DM rep2 from the analysis (Figure S10). These results strongly support the idea that KMT2A and KDM5C counteract to normalize H3K4me3 levels in specific genomic loci.

Peak annotation revealed that these genomic loci, which are misregulated in single mutants and rescued in DM, tend to be outside the promoters, such as distal intergenic regions, introns, and internal exons (Figure 6F). Examples of in such changes are represented in Figure S11. Finally, we tested whether the rescue effects in gene

expression involve normalization of H3K4me3. We took all rescued 2A-DEGs regardless of direction of changes in single mutants and plotted DM vs 2A fold changes of H3K4me3 as a function of DM vs 2A mRNA changes (Figure 6G and see method). Rescued 2A-DEGs mostly showed an increase in mRNA levels in DM (Q2 and Q4). When mRNA expression increases from 2A-HET to DM, H3K4me3 levels also tend to increase, which results in the larger number of genes within the upper right quadrant of the plot (Q2, 47 genes, $p < 1.0 \times 10^{-4}$, χ^2 test) compared to lower-right quadrant (Q4, 30 genes). Similarly, when mRNA expression decreases from 5C-KO to DM, the majority of genes are accompanied by decreased H3K4me3 nearby (Q3: 45 genes vs Q1: 20 genes, $p < 1.0 \times 10^{-4}$, χ^2 test). Furthermore, the magnitude of mRNA changes and H3K4me3 changes show positively correlation to some extent (Pearson $r = 0.16$, $p = 0.110$, and $r = 0.27$, $p = 0.020$ for 2A- and 5C-DEGs, respectively). Thus, misregulation of mRNA expression and its partial correction involve corresponding changes in the H3K4me3 levels.

Discussion

The present work, to our knowledge, represents the first genetic interactions between chromatin modification writer and eraser enzymes *in vivo*. Discovery of chromatin-modifying enzymes in the past decades made it clear that virtually no DNA- or histone-modifications are irreversible, and instead are subjected to dynamic regulation by writer and eraser enzymes. The genes encoding these enzymes appear to have undergone

duplication events during evolution. Complex organisms carry a greater number of genes that encode enzymes for single chromatin modification. For example, only one enzyme, Set1, is responsible for H3K4 methylation in fission yeast. In flies three genes, *Trx*, *Trr*, and *Set1* mediate H3K4me installation, and all three genes were duplicated in the mammalian genomes, which resulted in six SET-family H3K4 writers (67). A plethora of work has demonstrated specialized as well as redundant roles of individual histone-modifying enzymes within a family, in broad biological processes such as cancer and embryonic development (68). A fundamental question remained — is there any specific writer-eraser pairing in such highly duplicated gene families for a single chromatin modification? Mishra et al. showed that KDM5A antagonizes KMT2A, KMT2B, and KMT2D to modulate the transient site-specific DNA copy number gains in immortalized human cells (69). Cao et al. found that failed differentiation of mouse embryonic stem cells due to *Kmt2d* deletion can be rescued by *Kdm1a* knockdown (70). These pioneering efforts identified functional interplay between the opposing enzymes *in vitro*; however, no *in vivo* study has been reported. Thus, the present study substantially advances our understanding of how methyl-histone writer and eraser enzymes functionally interact during brain development and function.

Brain development is particularly relevant to the H3K4me dynamics, because a cohort of neurodevelopmental disorders have been genetically associated with impaired functions of these enzymes, as discussed earlier. Unlike previous studies using chemical approaches that block multiple chromatin regulators (19-21), we demonstrated that manipulation of a single enzyme, KMT2A or KDM5C, is sufficient to reverse many

neurological traits in both of the two single-mutant models. It may not be surprising that not all traits were reversed in DM mice, because compensatory actions by remaining H3K4me-regulators may potentially mediate these un-rescued traits. Our work opens a new avenue for future studies to delineate the full interplay between the 13 H3K4me-regulatory enzymes throughout brain development and function.

Several challenges remain, especially in linking molecular functions of KMT2A and KDM5C to cellular and behavioral outcomes. First, gene expression profiles did not perfectly correlate with cellular outcomes. While restorative effects on spine density were stronger in DM amygdala compared to hippocampus (Figure 4), the misregulation and rescue effects in the gene expression profile appear to be more pronounced in the hippocampus (Figure 5). One possible explanation is the difference in cell-type composition between the two brain regions, which is masked in our bulk tissue mRNA-seq. In addition, “causative” gene misregulation underlying cellular and behavioral traits may occur during a critical developmental time window and therefore not be sensitively captured in our study using adult brains. Second, histone modifying enzymes, including KDM5C, have been increasingly shown to exert their non-enzymatic function (27, 71-74). Third, although it has not been reported, there might be a non-histone substrate for KMT2A and KDM5C, as shown in other histone modifying enzymes (75). Finally, in a fly model of KMD5C-intellctual disability (76), impaired intestinal barrier and the altered microbiota appears to contribute to abnormal social behavior of the kdm5-mutant flies (77). One technical aspect is that while our RNA-seq was done primarily using 4–5-month-old animals, ChIP-seq was carried out using 8–14-month-old mice (Table S3).

Nonetheless, we found that the rescue effects in mRNA levels do involve H3K4me3 normalization (Figure 6G). Future studies are warranted to isolate the causal events between cell autonomous and non-cell autonomous mechanisms, enzymatic and non-enzymatic functions, and histone and non-histone substrates. The first step would be to test the functional contribution of candidate genes, many of which encode peptide-hormone signaling (Table 1), to the phenotypes in the single mutants and its rescue effect in DM mice.

Increased social dominance is a novel behavioral trait we observed in both WDSTS and MRXSCJ mouse models. The amygdala is well known to mediate social behaviors (78, 79). For example, lesions of BLA result in decreased aggression-like behavior and increased social interactions (80, 81), and changes in transcriptional regulation in BLA are observed after social interactions (79). The dorsal hippocampus CA1 is a direct recipient region of BLA inputs (48). Decreased BLA and CA1 spine densities in *Kmt2a*-HET and *Kdm5c*-KO mice inversely correlate with increased social dominance and aggression (Figures 4 and 6). Together, these observations imply that decreased spine density is not a cause of increased social dominance, but rather reflects compensatory reduction of net synaptic strength due to increased excitation and/or a loss of inhibitory control in this circuit. Thus, determining the connectivity of the amygdala with other regions, including prelimbic, infralimbic, and orbitofrontal cortices (82) as well as the ventral hippocampus, (78) will be critical for understanding the changes in social behaviors in both WDSTS and MRXSCJ models.

It is important to note that the double mutations introduced in our mice were constitutive, and therefore a lifetime of adaptation to loss of these two major chromatin regulators may occur from early developmental stages. A more realistic therapeutic strategy may be acute inhibition of KDM5C and KMT2A in the juvenile or mature brain. Previous work characterizing mouse models with excitatory-neuron specific ablation of *Kdm5c* or *Kmt2a* via *CamKII*-Cre found that conditional *Kmt2a* deletion led to clear learning deficits (30), while cognitive impairments in the conditional *Kdm5c*-KO mice were much milder than those of constitutive *Kdm5c*-KO mice (32). These results suggest a developmental origin of phenotypes in *Kdm5c*-KO. Future investigations are needed to address whether the effects of acute inhibition of opposing enzymes in these mouse models can restore such neurodevelopmental deficits.

Materials & methods

Mouse models

The *Kdm5c*-KO allele was previously described and maintained in C57BL/6J congenic background (31). *Kmt2a*-HET mice were generated by crossing previously described *Kmt2a*-flox (exons 8 and 9) mice with B6.129-Gt(ROSA)26Sor$^{tm1(cre/ERT2)Tyj}$/J-Cre mice (83). Our strategy was to use F1 hybrid for all studies as previously recommended as a standard practice to eliminate deleterious homozygous mutations, which can result in abnormalities in the congenic lines, e.g. deafness in C57/BL6 (84). We backcrossed *Kmt2a*$^{+/-}$ mice onto the desired 129S1/SvImJ strain, by marker-assisted accelerated backcrossing through Charles River Labs. *Kmt2a*$^{+/-}$ mice were bred to the N4 generation at minimum, where mice were >99% congenic for 129S1/SvImJ. All experimental mice were generated as F1 generation hybrids from mating between 129S1/SvImJ *Kmt2a*$^{+/-}$ males and C57Bl/6 *Kdm5c*$^{+/-}$ females: WT males (*Kmt2a*$^{+/+}$, *Kdm5c*$^{+/y}$); *Kdm5c*-KO males (*Kmt2a*$^{+/+}$, *Kdm5c*$^{-/y}$); *Kmt2a*-HET males (*Kmt2a*$^{+/-}$, *Kdm5c*$^{+/y}$); and *Kdm5c-Kmt2a*-DM males (*Kmt2a*$^{+/-}$, *Kdm5c*$^{-/y}$). Genotypes were confirmed using the following primers: for *Kmt2a*, 5'-GCCAGTCAGTCCGAAAGTAC, 5'-AGGATGTTCAAAGTGCCTGC, 5'-GCTCTAGAACTAGTGGATCCC; for *Kdm5c*, 5'-CAGGTGGCTTACTGTGACATTGATG, 5'-TGGGTTTGAGGGATACTTTAGG, 5'-GGTTCTCAACACTCACATAGTG.

Western blot analysis

Total proteins from adult brain tissues were subjected to Western blot analysis using in-house anti-KDM5C (31) and anti-GAPDH antibodies (G-9, Santa Cruz). For histone proteins, nuclei were enriched from the Dounce-homogenized brain tissues using Nuclei EZ prep Kit (Sigma, NUC-101). DNA were digested with micrococcal nuclease (MNase, NEB) for 10 minutes at room temperature, and total nuclear proteins were extracted by boiling the samples with the SDS-PAGE sample buffer. The following antibodies were used for Western blot analyses: anti-H3K4me3 (Abcam, ab8580), anti-H3K4me2 (Thermo, #710796), anti-H3K4me1 (Abcam, ab8895), and anti-H3 C-terminus (Millipore, CS204377).

Brain histology

Mice were subjected to transcardial perfusion according to standard procedures. Fixed brains were sliced on a freeze microtome, yielding 30 μm sections that were then fixed, permeabilized, blocked, and stained with DAPI. Slides were imaged on an Olympus SZX16 microscope, with an Olympus U-HGLGPS fluorescence source and Q Imaging Retiga 6000 camera. Images were captured using Q-Capture Pro 7 software. Data were collected in a blind fashion, where samples were coded and genotypes only revealed after data collection was complete.

Behavioral paradigms

Prior to behavioral testing, mice were acclimated to the animal colony room for one week single-housing in standard cages provided with a lab diet and water *ad libitum*. A 12-hour light-dark cycle (7:00AM-7:00PM) was utilized with temperature and humidity

maintained at 20 ±2 ºC and >30%, respectively. The University of Michigan Committee on the Use and Care of Animals approved all tests performed in this research. Five tests, listed in order of testing, were performed: Novel Object Recognition (five days), Context Fear Conditioning (two days), Three-Chambered Social Interaction (two days), Social Dominance Tube Test (three to four days), and Resident-intruder (two to three days). All testing was conducted in the morning by experimenters blind to genotype. The cleaning agent used in every test between each trial was 70% ethanol. Data were collected in a blind fashion, where mice were coded and genotypes were only revealed after testing was complete.

Novel Object Recognition: Mice were first habituated to testing arenas (40 x 30 x 32.5 cm^3) in three, 10-minute sessions over six consecutive days (85, 86). Twenty-four hours later, mice were allowed to explore two identical objects (a jar or egg, counterbalanced across animals) for two, 10-minute trials spaced three hours apart. All animals were returned to the arena, tested 24 hours after the first training session, and presented with one training object ("familiar" object: jar or egg) and one "novel" object (egg or jar). Exploration of the objects was defined as nose-point (sniffing) within 2 cm of the object. Behavior was automatically measured by Ethovision XT9 software using a Euresys Picolo U4H.264No/0 camera (Noldus, Cincinnati, OH). Preference was calculated as the time spent exploring novel object/total time exploring both objects. One-sample t-tests against 50% (no preference) were used to establish whether animals remembered the original objects.

Contextual Fear Conditioning: Context fear conditioning was assessed as previously described (87). Mice were placed into a distinct context with white walls (9 ¾ × 12 ¾ × 9 ¾ in) and a 36 steel rod grid floor (1/8 in diameter; ¼ spaced apart) (Med-Associates, St. Albans, VT) and allowed to explore for three minutes, followed by a two-second 0.8 mA shock, after which mice were immediately returned to their home cages in the colony room. Twenty-four hours later, mice were returned to the context and freezing behavior was assessed with NIR camera (VID-CAM-MONO-2A) and VideoFreeze (MedAssociates, St Albans, VT). Freezing levels were compared between genotypes using a between-groups analysis (one-way ANOVA) with genotype as the between-subjects factor.

Three-Chambered Social Interaction: Mice were placed into a three-chambered apparatus consisting of one central chamber (24 x 20 x 30 cm^3) and two identical side chambers (24.5 x 20 x 30 cm^3) each with a containment enclosure (8 cm diameter; 18 cm height; grey stainless steel grid 3 mm diameter spaced 7.4 mm apart) and allowed to habituate for 10 minutes. Twenty-four hours later, mice were returned to the apparatus that now included a 2-3 month-old stranger male mouse (C57BL/6N) on one side of the box (“stranger”), and a toy mouse approximately the same size and color as the stranger mouse on the other (“toy”). Exploration of either the stranger or toy was defined as nose-point (sniffing) within 2 cm of the enclosure and used as a measure of social interaction (88). Behavior was automatically scored by Ethovision XT9 software as described above, and social preference was defined as time exploring stranger/total exploration time. Social preference was analyzed using one-sample t-tests for each

genotype. A repeated measures analysis was used for each aggressive (genotype x aggression measures ANOVA) and submissive behavior (genotype x submissive) to analyze aggressive behaviors.

Social Dominance Tube Test: Twenty-four hours prior to testing, mice were habituated to a plastic clear cylindrical tube (1.5 in diameter; 50 cm length) for 10 minutes. During the test, two mice of different genotypes were placed at opposite ends of the tube and allowed to walk to the middle. The match concluded when the one mouse (the dominant mouse) forced the other mouse (the submissive mouse) to retreat with all four paws outside of the tube (a “win” for the dominant mouse) (89-91). Each mouse underwent a total of three matches against three different opponents for counterbalancing. Videos were recorded by Ethovision XT9 software as described above, and videos were manually scored by trained experimenters blind to genotype. The number of “wins” was reported as a percentage of total number of matches. Data were analyzed using an Exact Binomial Test with 0.5 as the probability of success (win or loss).

Resident-intruder aggression: Resident-intruder tests were used to assess aggression. Tests were performed on consecutive days, where the resident mouse was exposed to an unfamiliar intruder mouse for 15 minutes (92, 93). A trial was terminated prematurely if blood was drawn, if an attack lasted continuously for 30 seconds, or if an intruder showed visible signs of injury after an attack. Resident mice were assessed for active aggression (darting, mounting, chasing/following, tail rattling, and boxing/parrying), as well as submissive behaviors (cowering, upright, running away). Intruder mice were

assessed for passive defense (freezing, cowering, and digging). Behavior was recorded and videos scored manually by experimenters blind to genotype. Data were analyzed using a between-groups analysis (one-way ANOVA) with genotype as the between-subjects factor.

Neuronal Golgi staining and morphological analyses

Brains from adult (2-8 months) mice were dissected and incubated in a modified Golgi-Cox solution for two weeks at room temperature. The remaining procedure of Golgi immersion, cryosectioning, staining and coverslipping was performed as described previously (94).

Morphological analyses of dendrites were carried out as described previously (94). Four animals were used for each genotype, and pyramidal neurons in the basolateral amygdala and dorsal hippocampus CA1 per animal were quantified: N=24 neurons for WT, *Kmt2a*-HET and *Kdm5c*-KO, and N=27 neurons for DM. Quantification was done using commercially available software, NeuroLucida (v10, Microbrightfield, VT), installed on a Dell PC workstation that controlled a Zeiss Axioplan microscope with a CCD camera (1600 x 1200 pixels) and with a motorized X, Y, and Z focus for high-resolution image acquisition (100X oil immersion) and quantifications. The morphological analyses included: dendritic lengths, spine counts, and spine subtype morphology. All sample genotypes were blinded to the analysts throughout the course of the analysis.

The criteria for selecting candidate neurons for analysis were based on: (1) visualization of a completely filled soma with no overlap of neighboring soma and completely filled dendrites, (2) the tapering of most distal dendrites; and (3) the visualization of the complete 3-D profile of dendritic trees using the 3-D display of the imaging software.

For quantitative analysis of spine subtypes (thin, stubby, mushroom, filopodia, and branched spines), only spines orthogonal to the dendritic shaft were included in this analysis, whereas spines protruding above or beneath the dendritic shaft were not sampled. This principle remained consistent throughout the course of analysis.

After completion, the digital profile of neuron morphology was extrapolated and transported to a multi-panel computer workstation, then quantitated using NeuroExplorer program (Microbrightfield, VT), followed by statistical analysis (one- and two-way ANOVAs, $p < 0.05$).

RNA-seq

Brains from adult (4.5 to 8 months) male mice were microdissected to obtain the amygdala and hippocampus from Bregma ~ 4.80 mm regions. N=4 animals were used per genotype. The ages of mice used for genomics study, RNA-seq and ChIP-seq, are summarized in Table S3. Tissue was homogenized in Tri Reagent (Sigma). Samples were subjected to total RNA isolation, and RNA was purified using RNEasy Mini Kit (Qiagen). ERCC spike-in RNA was added at this stage, according to manufacturer's instructions (Life Technologies). Libraries were prepared using the NEBNext® Ultra™ II

Directional RNA Library Prep Kit with oligo-dT priming. Multiplexed libraries were pooled in approximately equimolar ratios and purified using Agencourt RNAClean XP beads (Beckman Coulter).

Libraries were sequenced on the Illumina Novaseq 6000 platform, with paired-end 150 base pair reads (24-35 million reads/library), according to standard procedures. Reads were mapped to the mm10 mouse genome (Gencode) using STAR (v2.5.3a) (95), where only uniquely mapped reads were used for downstream analyses. Duplicates were removed by STAR, and a counts file was generated using FeatureCounts (Subread v1.5.0) (96). BAM files were converted to bigwigs using deeptools (v3.1.3) (97, 98). Differentially expressed (DE) genes were called using DESeq2 (v1.14.1) (99, 100). Data analyses were performed with RStudio (v1.0.136). Fold change heatmaps was created using gplots heatmap.2 function.

To validate the microdissection of hippocampus and amygdala, we compared our RNA-seq datasets with similar RNA-seq data from Arbeitman (50) datasets, which involved the cerebellum, cortex, hippocampus, and amygdala. Briefly, count data underwent variance stabilizing transformation via DEseq2 vst function and Euclidean distances of the transformed values were calculated by dist command and the heatmap was generated by the pheatmap function. Linear regression analysis was performed using the smtr v3.4-8 slope.test function with intercept = FALSE and robust=FALSE options. Rescue-driving genes were chosen as genes that satisfy two conditions using R, **1)** abs (log2FC (single mutant vs DM) > 2, **2)** abs (log2FC (DM vs WT) < 0.7.

The RNA-seq data have been deposited in NCBI's Gene Expression Omnibus (101). Data are accessible through GEO series accession numbers, SuperSeries GSE127818 and SubSeries GSE127722, and can be accessed with secure token *ovuhykuazryxrad*.

ChIP-seq

Amygdala tissues were microdissected from adult (8-14.5 months) male mice. N=2 animals were used for WT, and N=3 animals were used for *Kmt2a*-HET, *Kdm5c*-KO, and DM as biological replicates. Nuclei were isolated using a Nuclei EZ prep Kit (Sigma, NUC-101), and counted after Trypan blue staining. Approximately 20,000 nuclei for each replicate were subjected to MNase digestion as previously described (102). We essentially followed the native ChIP-seq protocol (102) with two modifications. One was to use a kit to generate sequencing libraries in one-tube reactions (NEB, E7103S). Another modification was to spike-in the panel of synthetic nucleosomes carrying major histone methylations (EpiCypher, SKU: 19-1001) (66). For ChIP, we used the rabbit monoclonal H3K4me3 antibody (Thermo, clone #RM340).

Libraries were sequenced on the Illumina NextSeq 500 platform, with single-end 75 base-pair sequencing, according to standard procedures. We obtained 20-59 million reads per sample. Reads were aligned to the mm10 mouse genome (Gencode) and a custom genome containing the sequences from our standardized, synthetic nucleosomes (EpiCypher) for normalization (103), using Bowtie allowing up to two mismatches. Only uniquely mapped reads were used for analysis. The range of

uniquely mapped reads for input samples was 38-44 million reads. All IP replicates had a mean of 9.1 million uniquely mapped reads (range: 7.4-13.9 million). The enrichment of mapped synthetic spike-in nucleosomes compared to input was calculated and used as a normalization coefficient for read depth of each ChIP-seq replicate (103).

Peaks were called using MACS2 software (v 2.1.0.20140616) (104) using input BAM files for normalization, with filters for a q-value < 0.1 and a fold enrichment greater than 1. Common peak sets were obtained via DiffBind (105), and count tables for the common peaks were generated with the Bedtools multicov command. We removed "black-list" regions that often give aberrant signals (106). Resulting count tables were piped into DEseq2 to identify DMRs incorporating the synthetic nucleosome normalization into the read depth factor. We used ChIPseeker (107) to annotate H3K4me3 peaks with genomic features including mm10 promoters (defined here as ±1 kb from annotated transcription start site [TSS]). Normalized bam files were converted to bigwigs for visualization in the UCSC genome browser. Genes near peaks were identified by ChIPseeker. RNA-seq and ChIP-seq data were integrated using standard R commands and rescued amygdala DEGs were chosen as genes that meet two criteria, **1)** abs (log2FC (single mutant vs DM) > 1, **2)** abs (log2FC (DM vs WT) < 0.7. All scripts used in this study are available upon request.

The ChIP-seq data have been deposited in NCBI's Gene Expression Omnibus (101). Data are accessible through GEO series accession numbers, SuperSeries GSE127818 and SubSeries GSE127817, and can be accessed with secure token *ovuhykuazryxrad*.

Acknowledgements

We thank Dr. Ken Kwan, Mandy Lam, and Own Funk for their assistance with the RNA-seq library preparation protocol and use of their microscope; Chris Gates for his assistance with RNA-seq analyses; and Clara Farrehi, Jordan Rich, and Demetri Tsirukis for their assistance with experiments for transcriptome analyses, global histone methylation Western blots, and brain histology, respectively. We also thank Drs. Sally Camper, Stephen Parker, Stephanie Bielas, and Michael-Christopher Keogh, as well as the members of the Iwase and Bielas labs, for helpful discussions and critical review of the data.

Conflict of interest

MCW is CEO of Neurodigitech, LLC. The other authors declare no conflict of interest.

Author contributions

CNV, NCT, and SI conceived the study and designed the experiments. BR and KMC performed the mouse behavioral tests under the guidance of NCT. MCW oversaw dendritic morphometry analyses. CNV, KMB, PMG, and SI analyzed RNAseq data. YAS performed global H3K4me3 analyses. RSP and SI performed H3K4me3 ChIP-seq analyses. YD and CEK provided key experimental recourse and made important intellectual contributions. All authors contributed to the writing and editing of the manuscript.

Funding

This work was funded by an NIH National Research Service Award T32-GM07544 (University of Michigan Predoctoral Genetics Training Program) from the National Institute of General Medicine Sciences (to CNV), an NIH National Research Service Award T32-HD079342 (University of Michigan Predoctoral Career Training in the Reproductive Sciences Program) from the National Institute of Child Health and Human Development (NICHD) (to CNV), University of Michigan Rackham Predoctoral Research Grants (to CNV), a Michigan Institute for Clinical and Health Research fellowship (Translational Research Education Certificate, supported by UL1TR000433 and UL1TR002240) (to CNV), a University of Michigan Rackham Predoctoral Fellowship award (to CNV), an Autism Science Foundation Predoctoral Fellowship award (to CNV), an NIH National Research Service Award F31NS103377 from the National Institute of Neurological Disease & Stroke (NINDS) (to RSP), NIH NINDS Awards (R01NS089896 and R21NS104774) (to SI), Basil O'Connor Starter Scholar Research Awards from March of Dimes Foundation (to SI), and a Farrehi Family Foundation Grant (to SI).

Figures and Legends

Figure 1. The H3K4 methylopathies and generation of the *Kmt2a-Kdm5c* double-mutant (DM) mouse. (A) Histone H3 lysine 4 (H3K4me) methyltransferases (writers) and demethylases (erasers) depicted by their ability to place or remove H3K4me. Reader proteins recognizing specific H3K4me substrates (arrows) are depicted below. Genes are listed next to their associated neurodevelopmental disorder. KMT2A and KDM5C are highlighted in purple and green, respectively. WDSTS: Weideman-Steiner Syndrome; ID: intellectual disability; ASD: autism spectrum disorder, CPRF: cleft palate, psychomotor retardation, and distinctive facial features; ARID: autosomal recessive ID; MRXSCJ: mental retardation, X-linked, syndromic, Claes-Jensen type. **(B)** Mouse breeding scheme crossing congenic 129S1/SvlmJ *Kmt2a*-heterozygous males with congenic C57/Bl6 *Kdm5c*-heterozygous females, resulting in F1 generation mice. Only males were used in this study. **(C)** Numbers of male offspring across 30 litters, showing Mendelian ratios of expected genotypes. **(D)** Left panel: Body weight of adult mice > 2 months of age (mean ± SEM, ****$p < 0.0001$ in one-way ANOVA). Right panel: Difference between group means of weight (mean ± 95% confidence intervals, *$p<0.05$, **$p<0.01$, ***$p<0.001$, ****$p<0.0001$ in Tukey's multiple comparison test).

Figure 2. Deficit of memory-related behavior in *Kdm5c*-KO and its rescue in DM. (A) Contextual fear conditioning test. Left panel: Freezing levels after shock on test day (mean ± SEM, *$p < 0.05$ in one-way ANOVA). Right panel: Difference between group means of freezing (mean ± 95% confidence intervals, *$p<0.05$ in Least Significant Difference (LSD) test). **(B)** Novel object recognition test. Left panel: Preference for novel

versus familiar object (mean ± SEM, *p < 0.05 in one-way ANOVA). Right panel: Difference between group means of freeze response (mean ± 95% confidence intervals, *p<0.05 in Least Significant Difference (LSD) test). **(C)** Response to mild foot-shock (mean ± 95% confidence intervals, no statistical significance [n.s.], one-way ANOVA). **(D)** Locomotor activity (mean ± 95% confidence intervals, no statistical significance [n.s.], one-way ANOVA). N=21 WT, N=16 *Kmt2a*-HET, N=16 *Kdm5c*-KO, and N=12 DM animals were used for all studies.

Figure 3. Differential impacts of double mutation in social behavior. (A) Three chamber test for social interaction. Left panel: preference for stranger versus toy mouse (mean ± SEM, **p < 0.01 in one-way ANOVA). Right panel: Difference between group means of preference (mean ± 95% confidence intervals, *p<0.05, **p<0.01 in Least Significant Difference (LSD) test). **(B)** Tube test for social dominance. Proportion of wins in matches of each mutant versus WT. Numbers on colored bars represent total number of wins for WT (grey, above) or each mutant (below) in every matchup. **p<0.01, ***p<0.001, Exact binomial test. **(C)** Resident intruder test. Left panel: average number of all aggressive behaviors (mean ± SEM, *p < 0.05 in one-way ANOVA). Right panel: Difference between group means of aggressive behaviors (mean ± 95% confidence intervals, *p<0.05 in Least Significant Difference (LSD) test). N=21 WT, N=16 *Kmt2a*-HET, N=16 *Kdm5c*-KO, and N=12 DM animals were used for all studies.

Figure 4. Altered dendrite morphology of *Kdm5c*-KO and *Kmt2a*-HET was reversed in DM animals. (A) Representative images of basolateral amygdala (BLA)

pyramidal neurons across all genotypes, depicting overall neuron morphology including dendrite lengths and dendritic spines. Scale bars represent: 100μm (above, whole neuron image), 10μm (below, spine image). **(B and C)** Left panel: Total dendrite lengths **(B)** or spine density **(C)** (mean ± 95% *p<0.05, ****p<0.0001, one-way ANOVA). Right panel: Difference between group means (mean ± 95% confidence intervals, *p<0.05, **p<0.01, ***p<0.001, ****p<0.0001 in Tukey's multiple comparison test). **(D)** Quantification of spine morphology subtypes represented as percentage of total spines counted. **(E and F)** Morphometry of pyramidal neurons within the dorsal hippocampus CA1. At least 20 neurons from four animals per genotype were quantified for all panels.

Figure 5. The transcriptomes in the amygdala and hippocampus. (A) Number of differentially expressed (DE) genes across genotypes were determined using a threshold of *padj*-value < 0.1. or relaxed cut-off of p < 0.005 for *Kmt2a*-HET in **(B)** (see also Table S1). We analyzed amygdala and hippocampal tissues from four animals for each genotype. **(C)** Behavior of single-mutant DEGs in DM. Log2 fold change of DEGs relative to WT were plotted across the three mutants. Boxplot features: box, interquartile range (IQR); bold line, median; gray dots, individual genes. Associated p values result from Wilcoxon signed-rank tests. **(D)** Identification of rescue-driving genes and regression analysis. Blue fitting lines and slopes result from linear regression of log2 fold changes between the two genotypes. Gray shade: 95% confidence interval. *P*-values indicate probability of the null hypothesis that the fitting line does not differ from 1 (108). Red circles: rescue-driving genes (see method).

Figure 6. Altered H3K4me3 landscapes in the amygdala and rescue effect in DM. **(A)** Western blot of whole brain lysates showing unchanged global H3K4 methylation across genotypes. Total histone H3 was detected using an antibody recognizing the C-terminus of H3, and used as a control for equal loading. **(B)** PCA analysis of H3K4me3 ChIPseq replicates. We analyzed amygdala tissue from 2 to 3 animals (rep1-3) for each genotype (see Methods). **(C)** Number of H3K4me3 DMRs in 2a-HET, 5c-KO, or DM compared to WT across the genome. 2A-HET DMRs are retrieved with a relaxed threshold ($p < 0.05$). **(D)** Direction of H3K4me3 changes between single mutants. Genes are colored based on the direction of misregulation between the single mutants. **(E)** Behavior of single-mutant DMRs in DM. Log2 fold change of DMRs relative to WT were plotted across the three mutants. Boxplot features: box, interquartile range (IQR); bold line, median; gray dots, individual genes. Associated *p* values result from Wilcoxon signed-rank tests. **(F)** Genomic features of H3K4me3 peaks. **(G)** Involvement of H3K4me3 restoration near rescued DEGs. H3K4me3 log2 fold changes (FC) are plotted as function of mRNA log2 FC between DM and single mutants. Red line: linear regression fitting line with 95% confidence interval (gray shade). The gene numbers fall into each of the four quadrants as indicated (Q1-Q4). Results (*p*) of χ^2 test and Pearson's correlation coefficient (*r*) and p-value (*p*) are noted.

Supplementary Figure 1. Expression of KMT2A and KDM5C. (A) Expression of *Kmt2a* and *Kdm5c*, from FACS-sorted single cells of mouse visual cortex, shown in reads per kilobase of transcript per million mapped reads (RPKM). Neuronal cells:

GABAergic (GABA), Glutamatergic (Glu). Non-neuronal cells: astrocytes (A); endothelial cells (E); microglia (M), oligodendrocyte precursor cells (OPC); oligodendrocytes (O); smooth muscle cells (SMC). Image credit: Broad Institute "Single Cell Portal" transcriptome of adult mouse visual cortex (38). **(B)** Expression of *Kmt2a* and *Kdm5c* mRNA from adult mouse brain, shown in log2 of raw expression value from *in situ* hybridization. Brain regions: Isocortex, olfactory areas (OLF), hippocampal formation (HPF), cortical subplate (CTXsp), striatum (STR), pallidum (PAL), thalamus (TH), hypothalamus (HY), midbrain (MB), pons (P), medulla (MY), cerebellum (CB). Image credit: Allen Institute, Allen Mouse Brain Atlas (2004) (34). **(C)** Expression of *KMT2A* and *KDM5C* transcripts, from developing and adult human brains, shown in RPKM. Human development and adulthood were split into the following Periods: 1-7 fetal development; 8-9 birth and infancy; 10-11 childhood; 12 adolescence; and 13-15 adulthood. Image credit: Human Brain Transcriptome Atlas (36, 109)

Supplementary Figure 2. Basic features of mutant mice. (A-B) RNA-seq read coverage of *Kmt2a* **(A)** and *Kdm5c* **(B)** genes and targeted exons (highlight) confirmed the intended gene manipulations. **(C)** Genotyping using genomic DNA, confirming presence of *Kmt2a* and/or *Kdm5c* deleted alleles ("del") only in appropriate genotypes. **(D)** Western blot for KDM5C protein. Stars indicate non-specific bands present in all samples. GAPDH shown for equal loading. **(E)** Serial brain sections 30 μm thick stained with DAPI to mark nuclei. Sections shown at Bregma regions 1.41, 0.49, -2.15, and -2.91 mm (top to bottom). Regions highlighted: anterior forceps of the corpus callosum (fmi), caudate putamen (CPu), corpus callosum (cc), lateral ventricle (LV), piriform

cortex (Pir), olfactory tubercle (Tu), hippocampal fields CA1 and CA2, dentate gyrus (DG), anteromedial nucleus (AM), third ventricle (3V), substantia nigra pars reticularis (SNR). Scale bar: 1mm. **(F)** Body weight tracked from birth, postnatal day 1 (P1).

Supplementary Figure 3. Individual behavior types in the resident intruder test. **(A)** Individual aggressive behaviors (mean ± SEM, $^{**}p < 0.01$ in one-way ANOVA). N.S. depicts no statistical difference. Left panel: average number of all submissive behaviors (mean ± SEM, $^{*}p < 0.05$ in one-way ANOVA). Right panel: Difference between group means of submissive behaviors (mean ± 95% confidence intervals, $^{**}p<0.01$, $^{***}p<0.001$ in Least Significant Difference (LSD) test). **(B)** Individual submissive behaviors (mean ± SEM, $^{**}p < 0.01$ in one-way ANOVA). N.S. depicts no statistical difference. N=21 WT, N=16 *Kmt2a*-HET, N=16 *Kdm5c*-KO, and N=12 DM animals were used for all studies. Differences between group means all aggressive **(A)** and submissive **(B)** behaviors (mean ± 95% confidence intervals, $^{*}p<0.05$, $^{**}p<0.01$ in Least Significant Difference (LSD) test).

Supplementary Figure 4. Schematic of dendrite spine subtype analysis. (A) Projection image of a dendritic segment from a series of Z stack images derived from BLA pyramidal cells. Numerical marks adjacent to corresponding spine subtypes, represented as: 1. Filopodia, 2. Thin, 3, Stubby, 4. Mushroom, and 5. Branched.

Supplementary Figure 5. Validation of brain microdissection. (A) To validate accuracy of our brain microdissection, we compared our RNAseq data of the

hippocampus (HIP) and amygdala (AMY) with those of the Arbeitman paper (50), which involved the hippocampus (Hippo), amygdala (Amy), cerebellum (Cer), cerebral cortex (Ctx). Euclidian distance between all combination of RNA-seq data are plotted (see method). Samples from this study and the Arbeitman study are clustered separately, likely due to difference in experimental procedures and/or sex of mice. Our study used adult male mice, while the Arbeitman study used adult females. Nonetheless, our amygdala samples showed the shortest distance to the Arbeitman amygdala data compared to any other brain tissues (red rectangles). Likewise, our hippocampus data are closest to the Arbeitman hippocampus data among the four brain regions. The data demonstrate that the microdissection of brain regions in the two studies are consistent with each other.

Supplementary Figure 6. Basic analysis of RNA-seq data. (A) PCA analysis of RNA-seq libraries. Tissue types are a stronger segregating factor than genotypes. **(B)** Volcano plot representation of differential expressed genes (DEGs) in mutant vs WT comparisons. Red dots: DEGs with *padj* < 0.1 (see Table S1). **(C)** Mildly dysregulated genes in Kmt2a-HET were recovered with a relaxed threshold.

Supplementary Figure 7. Similarity of gene misregulation between the amygdala and hippocampus. (A) Overlap of single mutant DEGs between the amygdala (AMY) and hippocampus (HIP). 5C-DEGs overlap between the two brain regions. **(B)** Heatmap representation of log2 fold changes of 2A-DEGs (left) and 5C-DEGs (right). Overall the patterns of gene misregulation are similar in the two brain regions.

Supplementary Figure 8. Direction of gene misregulation between *Kmt2a*-HET and *Kdm5c*-KO and their overlap in DM brain tissues. (A) Behavior of single-mutant DEGs in the other single mutant. Log2 fold changes of DEGs found in a single mutant were plotted as a function of log2 fold changes in the other single mutant. Red shade covers genes that are regulated in the opposite direction between *Kmt2a*-HET and *Kdm5c*-KO brain tissues. Blue shade covers deregulated genes in the same direction. **(B)** The larger number of genes is dysregulated in the same direction between the two single mutants. **(C)** Overlap of DEGs between mutants. 5C- and DM-DEGs overlap substantially.

Supplementary Figure 9. Basic characterization of H3K4me3 ChIP-seq data. (A) Validation of H3K4me3 ChIP-seq specificity. Barcode reads originating from spike-in nucleosomes were counted. The two synthetic nucleosomes with the H3K4me3 barcodes dominated all ChIP samples, with H3K4me1/2 nucleosomes rarely detected. **(B)** Volcano plot represents the statistical significance of differentially methylated regions (DMRs). **(C)** MA plots of DMRs revealed signal intensity-dependent misregulation of H3K4me3 in *Kdm5c*-KO, where hypomethylated regions in the mutant were highly methylated in WT.

Supplementary Figure 10. Rescue effect without DM rep2. (A) DM rep2 showed strong rescue effect (Figure 6B). To test if H3K4me3 misregulations were alleviated in other DM replicates, we removed DM rep2 and then examined the behavior of single-

mutant DMRs in DM. Log2 fold change of DMRs relative to WT were plotted across the three mutants. Boxplot features: box, interquartile range (IQR); bold line, median; gray dots, individual genes. Associated *p* values result from Wilcoxon signed-rank tests. Rescue effects were still evident in DM and also dependent on the direction of misregulation between the single mutants.

Supplementary Figure 11. Representative loci found in the H3K4me3 ChIP-seq analysis. (A) Representative genome browser view of two representative loci for each of the major genome areas: rescued intergenic DMRs **(A)**, rescued promoter DMRs **(B)**, un-rescued DMRs **(C)**.

Gene symbol	Encoded protein	Chromosome	Description
Tacr1	Tachykinin receptor 1	chr6	Tachykinin receptor (aka neurokinin-1 or Substance-P receptor). G-protein coupled receptors found across the brain (110). Elevated *TACR1* mRNA levels in ASD patients with heightened aggression (111). Decreased aggression in *Tacr1*-KO mice (112).
Lhb	Beta subunit of luteinizing hormone (LH)	chr7	Major roles of LH in testosterone production (113). Additional roles of LH in learning and memory functions, e.g. elevated LH impairs spatial memory of rodents (114) and is associated with poor memory recall in men (115).
Trh	Thyrotropin-releasing hormone (TRH)	chr6	Primary TRH production in hypothalamic neurons. Some production and activity within the hippocampus (116). TRH stimulates GABA release within CA1 of the hippocampus (117). TRH increases during spatial learning tasks and is correlated with performance of rats (118).
Gabre	The epsilon subunit of the GABA-A	chrX	The epsilon subunit of GABA-A Receptor, an inhibitory chloride channel. Agonist-independent activity produces a tonic inhibitory tone onto neurons (119). Highest in the hypothalamus (120).
Adcy2	Adenylyl cyclase 2	chr13	Expressed at low levels throughout the brain and is stimulated by G-protein signaling and PKC (121). High expression in the soma and dendrites of hippocampal neurons and a proposed role in coincidence detection (122).
Adora2a	Adenosine A2a receptor	chr10	A G-protein coupled receptor of extracellular adenosine (123). A regulator of neurogenesis and hippocampal volume. Contribution of *ADORA2A* SNPs in Alzheimer's disease progression (124). Modulatory roles of BDNF expression and GABA and glutamate signaling in the hippocampus (125). Increased body mass, anxiety, and heightened aggression in *Adora2a*-KO mice (123).
Pomc	Pro-opiomelanocortin	chr12	A peptide hormone regulating the hypothalamic function such as feeding (58). High expression in the hypothalamus, and lower expression in the amygdala and hippocampus (58, 59). There, proposed roles in responding to stress (60). Impaired POMC expression in CA3 of the hippocampus is associated with cognitive decline in Alzheimer's disease (61).
Mc3r	Melanocortin 3 receptor	chr2	MC3R is receptor for cleavage products of POMC (64). Expression in the hypothalamus and limbic structures such as the amygdala and hippocampus (62). The hypothalamic function in weight and feeding (63). Roles in hippocampal memory consolidation (64).
Agt	Angiotensinogen	chr8	A peptide hormone primarily produced by astrocytes and converted into Angiotensin, neuroactive peptides (126). Well-known roles in vascular regulation, such as blood pressure (127). Angiotensin II inhibits LTP in the dentate gyrus in the hippocampus (128). Roles in mood and cognition (129).
P2ry14	Purinergic receptor P2Y, G-protein coupled	chr3	G-protein coupled receptor that binds UDP-glucose (130). Highly expressed in the placenta but moderately expressed in the brain (131). Upregulated in response to immune challenge and typically found within glia (130).

Table 1. Rescued 5C-DEGs that drove enrichment of the KEGG pathway "Neuroactive ligand-receptor interaction"

References

1. Faundes V, Newman WG, Bernardini L, Canham N, Clayton-Smith J, Dallapiccola B, et al. Histone Lysine Methylases and Demethylases in the Landscape of Human Developmental Disorders. *Am J Hum Genet.* 2018;102(1):175-87.
2. De Rubeis S, He X, Goldberg AP, Poultney CS, Samocha K, Ercument Cicek A, et al. Synaptic, transcriptional and chromatin genes disrupted in autism. *Nature.* 2014;515(7526):209-15.
3. Iossifov I, O'Roak BJ, Sanders SJ, Ronemus M, Krumm N, Levy D, et al. The contribution of de novo coding mutations to autism spectrum disorder. *Nature.* 2014;515(7526):216-21.
4. Kouzarides T. Chromatin modifications and their function. *Cell.* 2007;128(4):693-705.
5. Taverna SD, Li H, Ruthenburg AJ, Allis CD, and Patel DJ. How chromatin-binding modules interpret histone modifications: lessons from professional pocket pickers. *Nat Struct Mol Biol.* 2007;14(11):1025-40.
6. Allis CD, Berger SL, Cote J, Dent S, Jenuwien T, Kouzarides T, et al. New nomenclature for chromatin-modifying enzymes. *Cell.* 2007;131(4):633-6.
7. Iwase S, Berube NG, Zhou Z, Kasri NN, Battaglioli E, Scandaglia M, et al. Epigenetic Etiology of Intellectual Disability. *The Journal of neuroscience : the official journal of the Society for Neuroscience.* 2017;37(45):10773-82.
8. Ronan JL, Wu W, and Crabtree GR. From neural development to cognition: unexpected roles for chromatin. *Nat Rev Genet.* 2013;14(5):347-59.
9. Iwase S, and Shi Y. Histone and DNA modifications in mental retardation. *Progress in drug research Fortschritte der Arzneimittelforschung Progres des recherches pharmaceutiques.* 2011;67:147-73.
10. Barski A, Cuddapah S, Cui K, Roh TY, Schones DE, Wang Z, et al. High-resolution profiling of histone methylations in the human genome. *Cell.* 2007;129(4):823-37.
11. Heintzman ND, Stuart RK, Hon G, Fu Y, Ching CW, Hawkins RD, et al. Distinct and predictive chromatin signatures of transcriptional promoters and enhancers in the human genome. *Nat Genet.* 2007;39(3):311-8.
12. Vermeulen M, Mulder KW, Denissov S, Pijnappel WW, van Schaik FM, Varier RA, et al. Selective anchoring of TFIID to nucleosomes by trimethylation of histone H3 lysine 4. *Cell.* 2007;131(1):58-69.
13. Lauberth SM, Nakayama T, Wu X, Ferris AL, Tang Z, Hughes SH, et al. H3K4me3 Interactions with TAF3 Regulate Preinitiation Complex Assembly and Selective Gene Activation. *Cell.* 2013;152(5):1021-36.
14. Local A, Huang H, Albuquerque CP, Singh N, Lee AY, Wang W, et al. Identification of H3K4me1-associated proteins at mammalian enhancers. *Nat Genet.* 2018;50(1):73-82.
15. Cheung I, Shulha HP, Jiang Y, Matevossian A, Wang J, Weng Z, et al. Developmental regulation and individual differences of neuronal H3K4me3 epigenomes in the prefrontal cortex. *Proceedings of the National Academy of Sciences of the United States of America.* 2010;107(19):8824-9.

1050 16. Shulha HP, Cheung I, Whittle C, Wang J, Virgil D, Lin CL, et al. Epigenetic signatures
1051 of autism: trimethylated H3K4 landscapes in prefrontal neurons. *Arch Gen*
1052 *Psychiatry.* 2012;69(3):314-24.
1053 17. Shulha HP, Crisci JL, Reshetov D, Tushir JS, Cheung I, Bharadwaj R, et al. Human-
1054 specific histone methylation signatures at transcription start sites in prefrontal
1055 neurons. *PLoS biology.* 2012;10(11):e1001427.
1056 18. Vallianatos CN, and Iwase S. Disrupted intricacy of histone H3K4 methylation in
1057 neurodevelopmental disorders. *Epigenomics.* 2015;7(3):503-19.
1058 19. Alarcon JM, Malleret G, Touzani K, Vronskaya S, Ishii S, Kandel ER, et al. Chromatin
1059 acetylation, memory, and LTP are impaired in CBP+/- mice: a model for the
1060 cognitive deficit in Rubinstein-Taybi syndrome and its amelioration. *Neuron.*
1061 2004;42(6):947-59.
1062 20. Bjornsson HT, Benjamin JS, Zhang L, Weissman J, Gerber EE, Chen YC, et al. Histone
1063 deacetylase inhibition rescues structural and functional brain deficits in a mouse
1064 model of Kabuki syndrome. *Science translational medicine.* 2014;6(256):256ra135.
1065 21. Park J, Thomas S, and Munster PN. Epigenetic modulation with histone deacetylase
1066 inhibitors in combination with immunotherapy. *Epigenomics.* 2015;7(4):641-52.
1067 22. Strom SP, Lozano R, Lee H, Dorrani N, Mann J, O'Lague PF, et al. De Novo variants in
1068 the KMT2A (MLL) gene causing atypical Wiedemann-Steiner syndrome in two
1069 unrelated individuals identified by clinical exome sequencing. *BMC Med Genet.*
1070 2014;15:49.
1071 23. Jones WD, Dafou D, McEntagart M, Woollard WJ, Elmslie FV, Holder-Espinasse M, et
1072 al. De Novo Mutations in MLL Cause Wiedemann-Steiner Syndrome. *American*
1073 *Journal of Human Genetics.* 2012;91(2):358-64.
1074 24. Claes S, Devriendt K, Van Goethem G, Roelen L, Meireleire J, Raeymaekers P, et al.
1075 Novel syndromic form of X-linked complicated spastic paraplegia. *Am J Med Genet.*
1076 2000;94(1):1-4.
1077 25. Jensen LR, Amende M, Gurok U, Moser B, Gimmel V, Tzschach A, et al. Mutations in
1078 the JARID1C gene, which is involved in transcriptional regulation and chromatin
1079 remodeling, cause X-linked mental retardation. *Am J Hum Genet.* 2005;76(2):227-36.
1080 26. Adegbola A, Gao H, Sommer S, and Browning M. A novel mutation in JARID1C/SMCX
1081 in a patient with autism spectrum disorder (ASD). *American journal of medical*
1082 *genetics Part A.* 2008;146A(4):505-11.
1083 27. Vallianatos CN, Farrehi C, Friez MJ, Burmeister M, Keegan CE, and Iwase S. Altered
1084 Gene-Regulatory Function of KDM5C by a Novel Mutation Associated With Autism
1085 and Intellectual Disability. *Front Mol Neurosci.* 2018;11:104.
1086 28. Gupta S, Kim SY, Artis S, Molfese DL, Schumacher A, Sweatt JD, et al. Histone
1087 methylation regulates memory formation. *The Journal of neuroscience : the official*
1088 *journal of the Society for Neuroscience.* 2010;30(10):3589-99.
1089 29. Jakovcevski M, Ruan H, Shen EY, Dincer A, Javidfar B, Ma Q, et al. Neuronal
1090 Kmt2a/Mll1 histone methyltransferase is essential for prefrontal synaptic plasticity
1091 and working memory. *The Journal of neuroscience : the official journal of the Society*
1092 *for Neuroscience.* 2015;35(13):5097-108.
1093 30. Kerimoglu C, Sakib MS, Jain G, Benito E, Burkhardt S, Capece V, et al. KMT2A and
1094 KMT2B Mediate Memory Function by Affecting Distinct Genomic Regions. *Cell*
1095 *reports.* 2017;20(3):538-48.

1096 31. Iwase S, Brookes E, Agarwal S, Badeaux AI, Ito H, Vallianatos CN, et al. A Mouse
1097 Model of X-linked Intellectual Disability Associated with Impaired Removal of
1098 Histone Methylation. *Cell reports.* 2016.
1099 32. Scandaglia M, Lopez-Atalaya JP, Medrano-Fernandez A, Lopez-Cascales MT, Del
1100 Blanco B, Lipinski M, et al. Loss of Kdm5c Causes Spurious Transcription and
1101 Prevents the Fine-Tuning of Activity-Regulated Enhancers in Neurons. *Cell reports.*
1102 2017;21(1):47-59.
1103 33. Hawrylycz MJ, Lein ES, Guillozet-Bongaarts AL, Shen EH, Ng L, Miller JA, et al. An
1104 anatomically comprehensive atlas of the adult human brain transcriptome. *Nature.*
1105 2012;489(7416):391-9.
1106 34. Lein ES, Hawrylycz MJ, Ao N, Ayres M, Bensinger A, Bernard A, et al. Genome-wide
1107 atlas of gene expression in the adult mouse brain. *Nature.* 2007;445(7124):168-76.
1108 35. Zhang XQ, Wang ZL, Poon MW, and Yang JH. Spatial-temporal transcriptional
1109 dynamics of long non-coding RNAs in human brain. *Hum Mol Genet.*
1110 2017;26(16):3202-11.
1111 36. Pletikos M, Sousa AM, Sedmak G, Meyer KA, Zhu Y, Cheng F, et al. Temporal
1112 specification and bilaterality of human neocortical topographic gene expression.
1113 *Neuron.* 2014;81(2):321-32.
1114 37. Johnson MB, Kawasawa YI, Mason CE, Krsnik Z, Coppola G, Bogdanovic D, et al.
1115 Functional and evolutionary insights into human brain development through global
1116 transcriptome analysis. *Neuron.* 2009;62(4):494-509.
1117 38. Tasic B, Menon V, Nguyen TN, Kim TK, Jarsky T, Yao Z, et al. Adult mouse cortical cell
1118 taxonomy revealed by single cell transcriptomics. *Nature neuroscience.*
1119 2016;19(2):335-46.
1120 39. Cao F, Townsend EC, Karatas H, Xu J, Li L, Lee S, et al. Targeting MLL1 H3K4
1121 methyltransferase activity in mixed-lineage leukemia. *Mol Cell.* 2014;53(2):247-61.
1122 40. Wang F, Kessels HW, and Hu H. The mouse that roared: neural mechanisms of social
1123 hierarchy. *Trends Neurosci.* 2014;37(11):674-82.
1124 41. Kim B, Colon E, Chawla S, Vandenberg LN, and Suvorov A. Endocrine disruptors alter
1125 social behaviors and indirectly influence social hierarchies via changes in body
1126 weight. *Environ Health.* 2015;14:64.
1127 42. Varholick JA, Bailoo JD, Palme R, and Würbel H. Phenotypic variability between
1128 Social Dominance Ranks in laboratory mice. *Sci Rep.* 2018;8(1):6593.
1129 43. Penzes P, Cahill ME, Jones KA, VanLeeuwen JE, and Woolfrey KM. Dendritic spine
1130 pathology in neuropsychiatric disorders. *Nat Neurosci.* 2011;14(3):285-93.
1131 44. Dierssen M, and Ramakers GJ. Dendritic pathology in mental retardation: from
1132 molecular genetics to neurobiology. *Genes Brain Behav.* 2006;5 Suppl 2:48-60.
1133 45. Xu X, Miller EC, and Pozzo-Miller L. Dendritic spine dysgenesis in Rett syndrome.
1134 *Front Neuroanat.* 2014;8:97.
1135 46. Irwin SA, Galvez R, and Greenough WT. Dendritic spine structural anomalies in
1136 fragile-X mental retardation syndrome. *Cereb Cortex.* 2000;10(10):1038-44.
1137 47. Arikkath J. Molecular mechanisms of dendrite morphogenesis. *Front Cell Neurosci.*
1138 2012;6:61.
1139 48. Yang Y, and Wang JZ. From Structure to Behavior in Basolateral Amygdala-
1140 Hippocampus Circuits. *Front Neural Circuits.* 2017;11:86.

49. Jaworski E, and Routh A. ClickSeq: Replacing Fragmentation and Enzymatic Ligation with Click-Chemistry to Prevent Sequence Chimeras. *Methods Mol Biol.* 2018;1712:71-85.
50. Arbeitman MN. Maternal Experience Leads to Lasting Gene Expression Changes in Some Regions of the Mouse Brain. *G3 (Bethesda).* 2019;9(8):2623-8.
51. Dou YL, Milne TA, Ruthenburg AJ, Lee S, Lee JW, Verdine GL, et al. Regulation of MLL1 H3K4 methyltransferase activity by its core components. *Nature Structural & Molecular Biology.* 2006;13(8):713-9.
52. Zhang H, Gayen S, Xiong J, Zhou B, Shanmugam AK, Sun Y, et al. MLL1 Inhibition Reprograms Epiblast Stem Cells to Naive Pluripotency. *Cell stem cell.* 2016;18(4):481-94.
53. Iwase S, Lan F, Bayliss P, de la Torre-Ubieta L, Huarte M, Qi HH, et al. The X-linked mental retardation gene SMCX/JARID1C defines a family of histone H3 lysine 4 demethylases. *Cell.* 2007;128(6):1077-88.
54. Outchkourov NS, Muino JM, Kaufmann K, van Ijcken WF, Groot Koerkamp MJ, van Leenen D, et al. Balancing of histone H3K4 methylation states by the Kdm5c/SMCX histone demethylase modulates promoter and enhancer function. *Cell reports.* 2013;3(4):1071-9.
55. S G, E M, Y M-N, CN V, RS P, PM G, et al. biorxiv: Cold Spring Harbor Laboratory; 2017.
56. Chen EY, Tan CM, Kou Y, Duan Q, Wang Z, Meirelles GV, et al. Enrichr: interactive and collaborative HTML5 gene list enrichment analysis tool. *BMC bioinformatics.* 2013;14:128.
57. Kuleshov MV, Jones MR, Rouillard AD, Fernandez NF, Duan Q, Wang Z, et al. Enrichr: a comprehensive gene set enrichment analysis web server 2016 update. *Nucleic acids research.* 2016;44(W1):W90-7.
58. Civelli O, Birnberg N, and Herbert E. Detection and quantitation of pro-opiomelanocortin mRNA in pituitary and brain tissues from different species. *The Journal of biological chemistry.* 1982;257(12):6783-7.
59. Pałasz A, Bandyszewska M, Rojczyk E, and Wiaderkiewicz R. Effect of extended olanzapine administration on POMC and neuropeptide Y mRNA levels in the male rat amygdala and hippocampus. *Pharmacol Rep.* 2016;68(2):292-6.
60. Niikura K, Zhou Y, Ho A, and Kreek MJ. Proopiomelanocortin (POMC) expression and conditioned place aversion during protracted withdrawal from chronic intermittent escalating-dose heroin in POMC-EGFP promoter transgenic mice. *Neuroscience.* 2013;236:220-32.
61. Shen Y, Tian M, Zheng Y, Gong F, Fu AKY, and Ip NY. Stimulation of the Hippocampal POMC/MC4R Circuit Alleviates Synaptic Plasticity Impairment in an Alzheimer's Disease Model. *Cell reports.* 2016;17(7):1819-31.
62. Roselli-Rehfuss L, Mountjoy KG, Robbins LS, Mortrud MT, Low MJ, Tatro JB, et al. Identification of a receptor for gamma melanotropin and other proopiomelanocortin peptides in the hypothalamus and limbic system. *Proceedings of the National Academy of Sciences of the United States of America.* 1993;90(19):8856-60.

1185 63. Pei H, Patterson CM, Sutton AK, Burnett KH, Myers MG, and Olson DP. Lateral
1186 Hypothalamic Mc3R-Expressing Neurons Modulate Locomotor Activity, Energy
1187 Expenditure, and Adiposity in Male Mice. *Endocrinology.* 2019;160(2):343-58.
1188 64. Machado I, González P, Schiöth HB, Lasaga M, and Scimonelli TN. α-Melanocyte-
1189 stimulating hormone (α-MSH) reverses impairment of memory reconsolidation
1190 induced by interleukin-1 beta (IL-1 beta) hippocampal infusions. *Peptides.*
1191 2010;31(11):2141-4.
1192 65. Tahiliani M, Mei PC, Fang R, Leonor T, Rutenberg M, Shimizu F, et al. The histone
1193 H3K4 demethylase SMCX links REST target genes to X-linked mental retardation.
1194 *Nature.* 2007;447(7144):601-+.
1195 66. Shah RN, Grzybowski AT, Cornett EM, Johnstone AL, Dickson BM, Boone BA, et al.
1196 Examining the Roles of H3K4 Methylation States with Systematically Characterized
1197 Antibodies. *Molecular cell.* 2018;72(1):162-77 e7.
1198 67. Eissenberg JC, and Shilatifard A. Histone H3 lysine 4 (H3K4) methylation in
1199 development and differentiation. *Dev Biol.* 2010;339(2):240-9.
1200 68. Shilatifard A. The COMPASS family of histone H3K4 methylases: mechanisms of
1201 regulation in development and disease pathogenesis. *Annual review of biochemistry.*
1202 2012;81:65-95.
1203 69. Mishra S, Van Rechem C, Pal S, Clarke TL, Chakraborty D, Mahan SD, et al. Cross-talk
1204 between Lysine-Modifying Enzymes Controls Site-Specific DNA Amplifications. *Cell.*
1205 2018;175(6):1716.
1206 70. Cao K, Collings CK, Morgan MA, Marshall SA, Rendleman EJ, Ozark PA, et al. An
1207 Mll4/COMPASS-Lsd1 epigenetic axis governs enhancer function and pluripotency
1208 transition in embryonic stem cells. *Sci Adv.* 2018;4(1):eaap8747.
1209 71. Liu X, and Secombe J. The Histone Demethylase KDM5 Activates Gene Expression by
1210 Recognizing Chromatin Context through Its PHD Reader Motif. *Cell reports.*
1211 2015;13(10):2219-31.
1212 72. Dimitrova E, Turberfield AH, and Klose RJ. Histone demethylases in chromatin
1213 biology and beyond. *EMBO Rep.* 2015;16(12):1620-39.
1214 73. Dorighi KM, Swigut T, Henriques T, Bhanu NV, Scruggs BS, Nady N, et al. Mll3 and
1215 Mll4 Facilitate Enhancer RNA Synthesis and Transcription from Promoters
1216 Independently of H3K4 Monomethylation. *Molecular cell.* 2017;66(4):568-76 e4.
1217 74. Aubert Y, Egolf S, and Capell BC. The Unexpected Noncatalytic Roles of Histone
1218 Modifiers in Development and Disease. *Trends Genet.* 2019;35(9):645-57.
1219 75. Zhang X, Wen H, and Shi X. Lysine methylation: beyond histones. *Acta Biochim*
1220 *Biophys Sin (Shanghai).* 2012;44(1):14-27.
1221 76. Zamurrad S, Hatch HAM, Drelon C, Belalcazar HM, and Secombe J. A Drosophila
1222 Model of Intellectual Disability Caused by Mutations in the Histone Demethylase
1223 KDM5. *Cell reports.* 2018;22(9):2359-69.
1224 77. Chen K, Luan X, Liu Q, Wang J, Chang X, Snijders AM, et al. Drosophila Histone
1225 Demethylase KDM5 Regulates Social Behavior through Immune Control and Gut
1226 Microbiota Maintenance. *Cell Host Microbe.* 2019;25(4):537-52 e8.
1227 78. Felix-Ortiz AC, and Tye KM. Amygdala inputs to the ventral hippocampus
1228 bidirectionally modulate social behavior. *J Neurosci.* 2014;34(2):586-95.
1229 79. McCann KE, Sinkiewicz DM, Rosenhauer AM, Beach LQ, and Huhman KL.
1230 Transcriptomic Analysis Reveals Sex-Dependent Expression Patterns in the

Basolateral Amygdala of Dominant and Subordinate Animals After Acute Social Conflict. *Mol Neurobiol.* 2018.

80. Levinson DM, Reeves DL, and Buchanan DR. Reductions in aggression and dominance status in guinea pigs following bilateral lesions in the basolateral amygdala or lateral septum. *Physiol Behav.* 1980;25(6):963-71.

81. McGregor A, and Herbert J. Differential effects of excitotoxic basolateral and corticomedial lesions of the amygdala on the behavioural and endocrine responses to either sexual or aggression-promoting stimuli in the male rat. *Brain Res.* 1992;574(1-2):9-20.

82. Felix-Ortiz AC, Burgos-Robles A, Bhagat ND, Leppla CA, and Tye KM. Bidirectional modulation of anxiety-related and social behaviors by amygdala projections to the medial prefrontal cortex. *Neuroscience.* 2016;321:197-209.

83. McMahon KA, Hiew SY, Hadjur S, Veiga-Fernandes H, Menzel U, Price AJ, et al. Mll has a critical role in fetal and adult hematopoietic stem cell self-renewal. *Cell stem cell.* 2007;1(3):338-45.

84. Silva AJ, Simpson EM, Takahashi JS, Lipp HP, Nakanishi S, Wehner JM, et al. Mutant mice and neuroscience: recommendations concerning genetic background. Banbury Conference on genetic background in mice. *Neuron.* 1997;19(4):755-9.

85. Vogel-Ciernia A, and Wood MA. Examining object location and object recognition memory in mice. *Curr Protoc Neurosci.* 2014;69:8.31.1-17.

86. Tchessalova D, and Tronson NC. Memory deficits in males and females long after subchronic immune challenge. *Neurobiol Learn Mem.* 2019.

87. Keiser AA, Turnbull LM, Darian MA, Feldman DE, Song I, and Tronson NC. Sex Differences in Context Fear Generalization and Recruitment of Hippocampus and Amygdala during Retrieval. *Neuropsychopharmacology : official publication of the American College of Neuropsychopharmacology.* 2017;42(2):397-407.

88. Crawley JN. Mouse behavioral assays relevant to the symptoms of autism. *Brain Pathol.* 2007;17(4):448-59.

89. Zhou T, Zhu H, Fan Z, Wang F, Chen Y, Liang H, et al. History of winning remodels thalamo-PFC circuit to reinforce social dominance. *Science.* 2017;357(6347):162-8.

90. Larrieu T, Cherix A, Duque A, Rodrigues J, Lei H, Gruetter R, et al. Hierarchical Status Predicts Behavioral Vulnerability and Nucleus Accumbens Metabolic Profile Following Chronic Social Defeat Stress. *Curr Biol.* 2017;27(14):2202-10.e4.

91. Moretti P, Bouwknecht JA, Teague R, Paylor R, and Zoghbi HY. Abnormalities of social interactions and home-cage behavior in a mouse model of Rett syndrome. *Hum Mol Genet.* 2005;14(2):205-20.

92. Guzmán YF, Tronson NC, Jovasevic V, Sato K, Guedea AL, Mizukami H, et al. Fear-enhancing effects of septal oxytocin receptors. *Nat Neurosci.* 2013;16(9):1185-7.

93. Miczek KA, Maxson SC, Fish EW, and Faccidomo S. Aggressive behavioral phenotypes in mice. *Behav Brain Res.* 2001;125(1-2):167-81.

94. Shmelkov SV, Hormigo A, Jing D, Proenca CC, Bath KG, Milde T, et al. Slitrk5 deficiency impairs corticostriatal circuitry and leads to obsessive-compulsive-like behaviors in mice. *Nature medicine.* 2010;16(5):598-602, 1p following

95. Dobin A, Davis CA, Schlesinger F, Drenkow J, Zaleski C, Jha S, et al. STAR: ultrafast universal RNA-seq aligner. *Bioinformatics.* 2013;29(1):15-21.

96. Liao Y, Smyth GK, and Shi W. featureCounts: an efficient general purpose program for assigning sequence reads to genomic features. *Bioinformatics.* 2014;30(7):923-30.
97. Ramírez F, Dündar F, Diehl S, Grüning BA, and Manke T. deepTools: a flexible platform for exploring deep-sequencing data. *Nucleic Acids Res.* 2014;42(Web Server issue):W187-91.
98. Ramírez F, Ryan DP, Grüning B, Bhardwaj V, Kilpert F, Richter AS, et al. deepTools2: a next generation web server for deep-sequencing data analysis. *Nucleic Acids Res.* 2016;44(W1):W160-5.
99. Anders S, and Huber W. Differential expression analysis for sequence count data. *Genome biology.* 2010;11(10):R106.
100. Love MI, Huber W, and Anders S. Moderated estimation of fold change and dispersion for RNA-seq data with DESeq2. *Genome Biol.* 2014;15(12):550.
101. Edgar R, Domrachev M, and Lash AE. Gene Expression Omnibus: NCBI gene expression and hybridization array data repository. *Nucleic Acids Res.* 2002;30(1):207-10.
102. Brind'Amour J, Liu S, Hudson M, Chen C, Karimi MM, and Lorincz MC. An ultra-low-input native ChIP-seq protocol for genome-wide profiling of rare cell populations. *Nat Commun.* 2015;6:6033.
103. Grzybowski AT, Chen Z, and Ruthenburg AJ. Calibrating ChIP-Seq with Nucleosomal Internal Standards to Measure Histone Modification Density Genome Wide. *Molecular cell.* 2015;58(5):886-99.
104. Zhang Y, Liu T, Meyer CA, Eeckhoute J, Johnson DS, Bernstein BE, et al. Model-based analysis of ChIP-Seq (MACS). *Genome biology.* 2008;9(9):R137.
105. Ross-Innes CS, Stark R, Teschendorff AE, Holmes KA, Ali HR, Dunning MJ, et al. Differential oestrogen receptor binding is associated with clinical outcome in breast cancer. *Nature.* 2012;481(7381):389-93.
106. Amemiya HM, Kundaje A, and Boyle AP. The ENCODE Blacklist: Identification of Problematic Regions of the Genome. *Sci Rep.* 2019;9(1):9354.
107. Yu G, Wang LG, and He QY. ChIPseeker: an R/Bioconductor package for ChIP peak annotation, comparison and visualization. *Bioinformatics.* 2015;31(14):2382-3.
108. Warton DI, Wright IJ, Falster DS, and Westoby M. Bivariate line-fitting methods for allometry. *Biol Rev Camb Philos Soc.* 2006;81(2):259-91.
109. Kang HJ, Kawasawa YI, Cheng F, Zhu Y, Xu X, Li M, et al. Spatio-temporal transcriptome of the human brain. *Nature.* 2011;478(7370):483-9.
110. Rigby M, O'Donnell R, and Rupniak NM. Species differences in tachykinin receptor distribution: further evidence that the substance P (NK1) receptor predominates in human brain. *The Journal of comparative neurology.* 2005;490(4):335-53.
111. Sener EF, Taheri S, Sahin MC, Bayramov KK, Marasli MK, Zararsiz G, et al. Altered Global mRNA Expressions of Pain and Aggression Related Genes in the Blood of Children with Autism Spectrum Disorders. *J Mol Neurosci.* 2019;67(1):89-96.
112. De Felipe C, Herrero JF, O'Brien JA, Palmer JA, Doyle CA, Smith AJ, et al. Altered nociception, analgesia and aggression in mice lacking the receptor for substance P. *Nature.* 1998;392(6674):394-7.

113. Huhtaniemi I, Zhang FP, Kero J, Hamalainen T, and Poutanen M. Transgenic and knockout mouse models for the study of luteinizing hormone and luteinizing hormone receptor function. *Mol Cell Endocrinol.* 2002;187(1-2):49-56.
114. Burnham V, Sundby C, Laman-Maharg A, and Thornton J. Luteinizing hormone acts at the hippocampus to dampen spatial memory. *Horm Behav.* 2017;89:55-63.
115. Hyde Z, Flicker L, Almeida OP, McCaul KA, Jamrozik K, Hankey GJ, et al. Higher luteinizing hormone is associated with poor memory recall: the health in men study. *J Alzheimers Dis.* 2010;19(3):943-51.
116. Low WC, Roepke J, Farber SD, Hill TG, Sattin A, and Kubek MJ. Distribution of thyrotropin-releasing hormone (TRH) in the hippocampal formation as determined by radioimmunoassay. *Neuroscience letters.* 1989;103(3):314-9.
117. Deng PY, Porter JE, Shin HS, and Lei S. Thyrotropin-releasing hormone increases GABA release in rat hippocampus. *The Journal of physiology.* 2006;577(Pt 2):497-511.
118. Aguilar-Valles A, Sánchez E, de Gortari P, García-Vazquez AI, Ramírez-Amaya V, Bermúdez-Rattoni F, et al. The expression of TRH, its receptors and degrading enzyme is differentially modulated in the rat limbic system during training in the Morris water maze. *Neurochemistry international.* 2007;50(2):404-17.
119. Neelands TR, Fisher JL, Bianchi M, and Macdonald RL. Spontaneous and gamma-aminobutyric acid (GABA)-activated GABA(A) receptor channels formed by epsilon subunit-containing isoforms. *Molecular pharmacology.* 1999;55(1):168-78.
120. Mehta AK, and Ticku MK. An update on GABAA receptors. *Brain Res Brain Res Rev.* 1999;29(2-3):196-217.
121. Mons N, Harry A, Dubourg P, Premont RT, Iyengar R, and Cooper DM. Immunohistochemical localization of adenylyl cyclase in rat brain indicates a highly selective concentration at synapses. *Proceedings of the National Academy of Sciences of the United States of America.* 1995;92(18):8473-7.
122. Baker LP, Nielsen MD, Impey S, Hacker BM, Poser SW, Chan MY, et al. Regulation and immunohistochemical localization of betagamma-stimulated adenylyl cyclases in mouse hippocampus. *The Journal of neuroscience : the official journal of the Society for Neuroscience.* 1999;19(1):180-92.
123. Ledent C, Vaugeois JM, Schiffmann SN, Pedrazzini T, El Yacoubi M, Vanderhaeghen JJ, et al. Aggressiveness, hypoalgesia and high blood pressure in mice lacking the adenosine A2a receptor. *Nature.* 1997;388(6643):674-8.
124. Horgusluoglu-Moloch E, Nho K, Risacher SL, Kim S, Foroud T, Shaw LM, et al. Targeted neurogenesis pathway-based gene analysis identifies ADORA2A associated with hippocampal volume in mild cognitive impairment and Alzheimer's disease. *Neurobiology of aging.* 2017;60:92-103.
125. Vaz SH, Lérias SR, Parreira S, Diógenes MJ, and Sebastião AM. Adenosine A2A receptor activation is determinant for BDNF actions upon GABA and glutamate release from rat hippocampal synaptosomes. *Purinergic Signal.* 2015;11(4):607-12.
126. O'Caoimh R, Kehoe PG, and Molloy DW. Renin Angiotensin aldosterone system inhibition in controlling dementia-related cognitive decline. *J Alzheimers Dis.* 2014;42 Suppl 4:S575-86.
127. Jackson L, Eldahshan W, Fagan SC, and Ergul A. Within the Brain: The Renin Angiotensin System. *Int J Mol Sci.* 2018;19(3).

128. Denny JB, Polan-Curtain J, Wayner MJ, and Armstrong DL. Angiotensin II blocks hippocampal long-term potentiation. *Brain research.* 1991;567(2):321-4.
129. Wayner MJ, Armstrong DL, Polan-Curtain JL, and Denny JB. Role of angiotensin II and AT1 receptors in hippocampal LTP. *Pharmacol Biochem Behav.* 1993;45(2):455-64.
130. Abbracchio MP, Boeynaems JM, Barnard EA, Boyer JL, Kennedy C, Miras-Portugal MT, et al. Characterization of the UDP-glucose receptor (re-named here the P2Y14 receptor) adds diversity to the P2Y receptor family. *Trends Pharmacol Sci.* 2003;24(2):52-5.
131. Chambers JK, Macdonald LE, Sarau HM, Ames RS, Freeman K, Foley JJ, et al. A G protein-coupled receptor for UDP-glucose. *The Journal of biological chemistry.* 2000;275(15):10767-71.

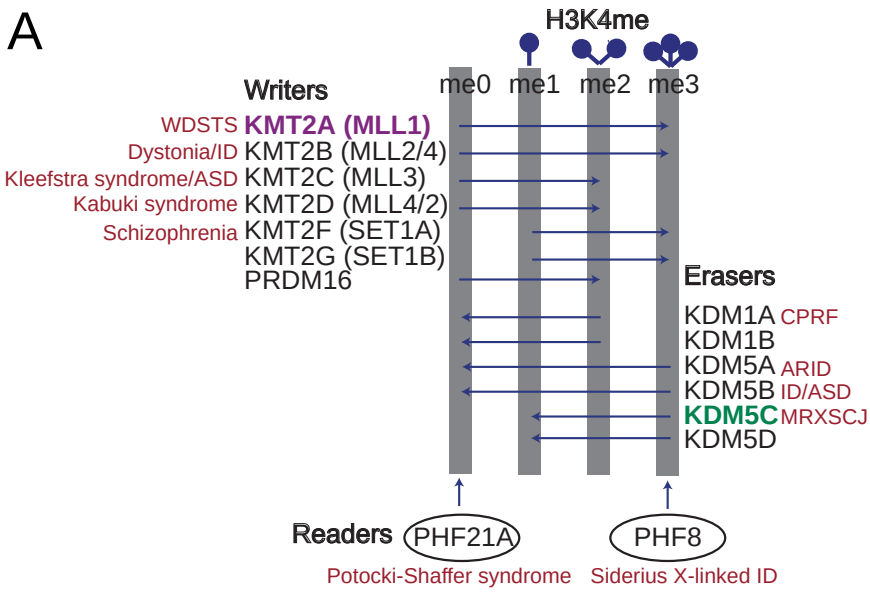

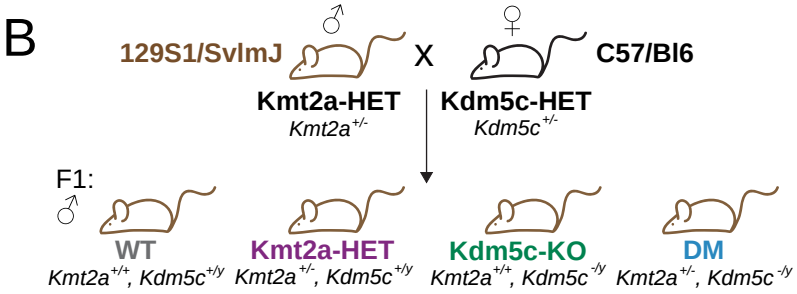

C

Number of offspring across 30 litters (% total males)			
WT	2a-HET	5c-KO	DM
17	16	21	14
(25%)	(23%)	(31%)	(21%)

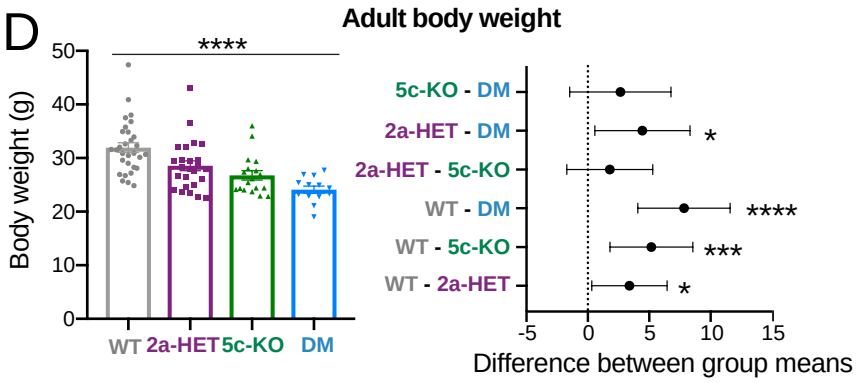

Figure 1

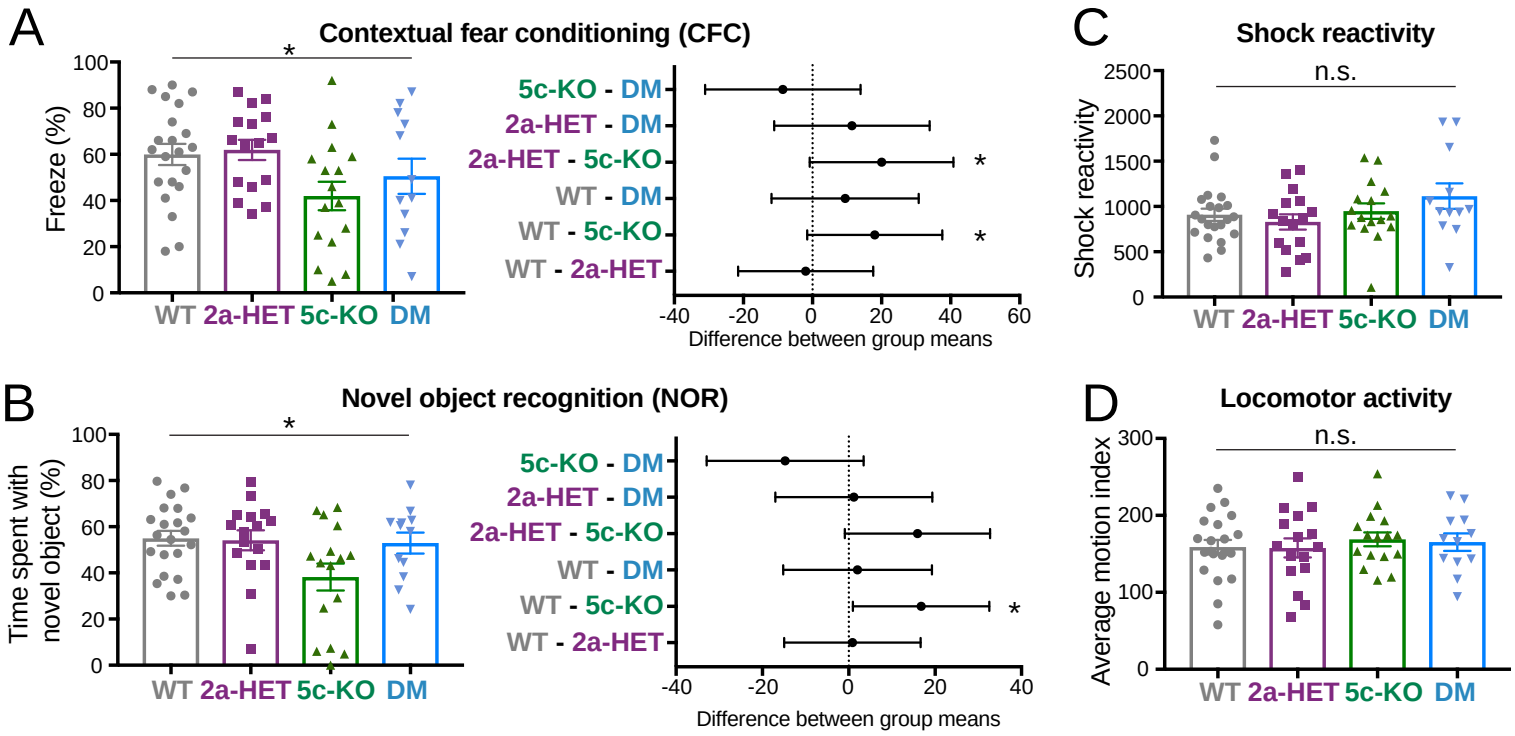
A
Contextual fear conditioning (CFC)
Freeze (%)
100
80
60
40
20
0
*
WT 2a-HET 5c-KO DM
5c-KO - DM
2a-HET - DM
2a-HET - 5c-KO
WT - DM
WT - 5c-KO
WT - 2a-HET
*
*
-40 -20 0 20 40 60
Difference between group means
C
Shock reactivity
Shock reactivity
2500
2000
1500
1000
500
0
n.s.
WT 2a-HET 5c-KO DM
B
Novel object recognition (NOR)
Time spent with novel object (%)
100
80
60
40
20
0
*
WT 2a-HET 5c-KO DM
5c-KO - DM
2a-HET - DM
2a-HET - 5c-KO
WT - DM
WT - 5c-KO
WT - 2a-HET
*
-40 -20 0 20 40
Difference between group means
D
Locomotor activity
Average motion index
300
200
100
0
n.s.
WT 2a-HET 5c-KO DM

Figure 2

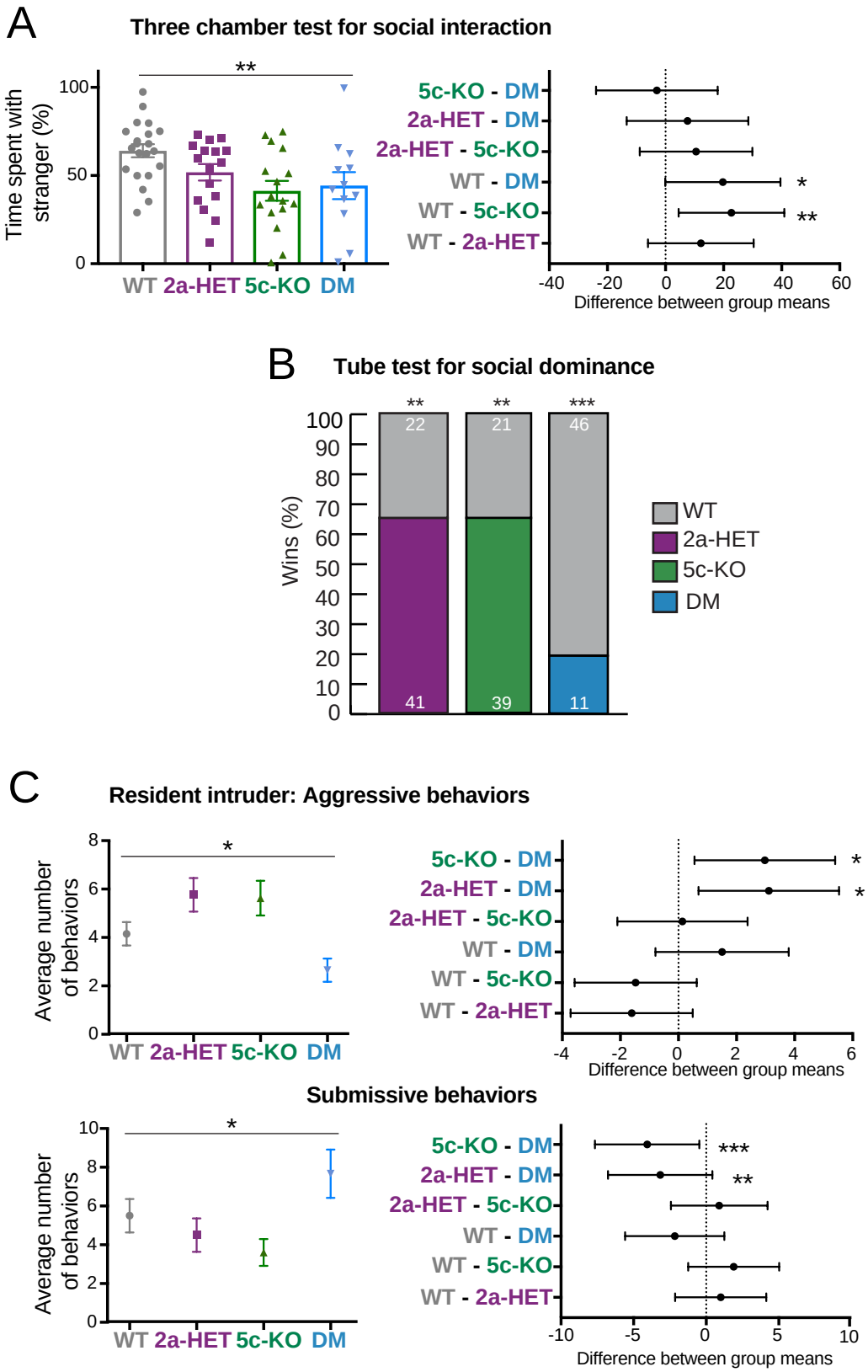
A
Three chamber test for social interaction
Time spent with stranger (%)
100
50
0
**
WT 2a-HET 5c-KO DM
5c-KO - DM
2a-HET - DM
2a-HET - 5c-KO
WT - DM
WT - 5c-KO
WT - 2a-HET
*
**
-40 -20 0 20 40 60
Difference between group means
B
Tube test for social dominance
Wins (%)
100 90 80 70 60 50 40 30 20 10 0
** ** ***
22 21 46
41 39 11
WT
2a-HET
5c-KO
DM
C
Resident intruder: Aggressive behaviors
Average number of behaviors
8 6 4 2 0
*
WT 2a-HET 5c-KO DM
5c-KO - DM
2a-HET - DM
2a-HET - 5c-KO
WT - DM
WT - 5c-KO
WT - 2a-HET
*
*
-4 -2 0 2 4 6
Difference between group means
Submissive behaviors
Average number of behaviors
10 8 6 4 2 0
*
WT 2a-HET 5c-KO DM
5c-KO - DM
2a-HET - DM
2a-HET - 5c-KO
WT - DM
WT - 5c-KO
WT - 2a-HET
***
**
-10 -5 0 5 10
Difference between group means

Figure 3

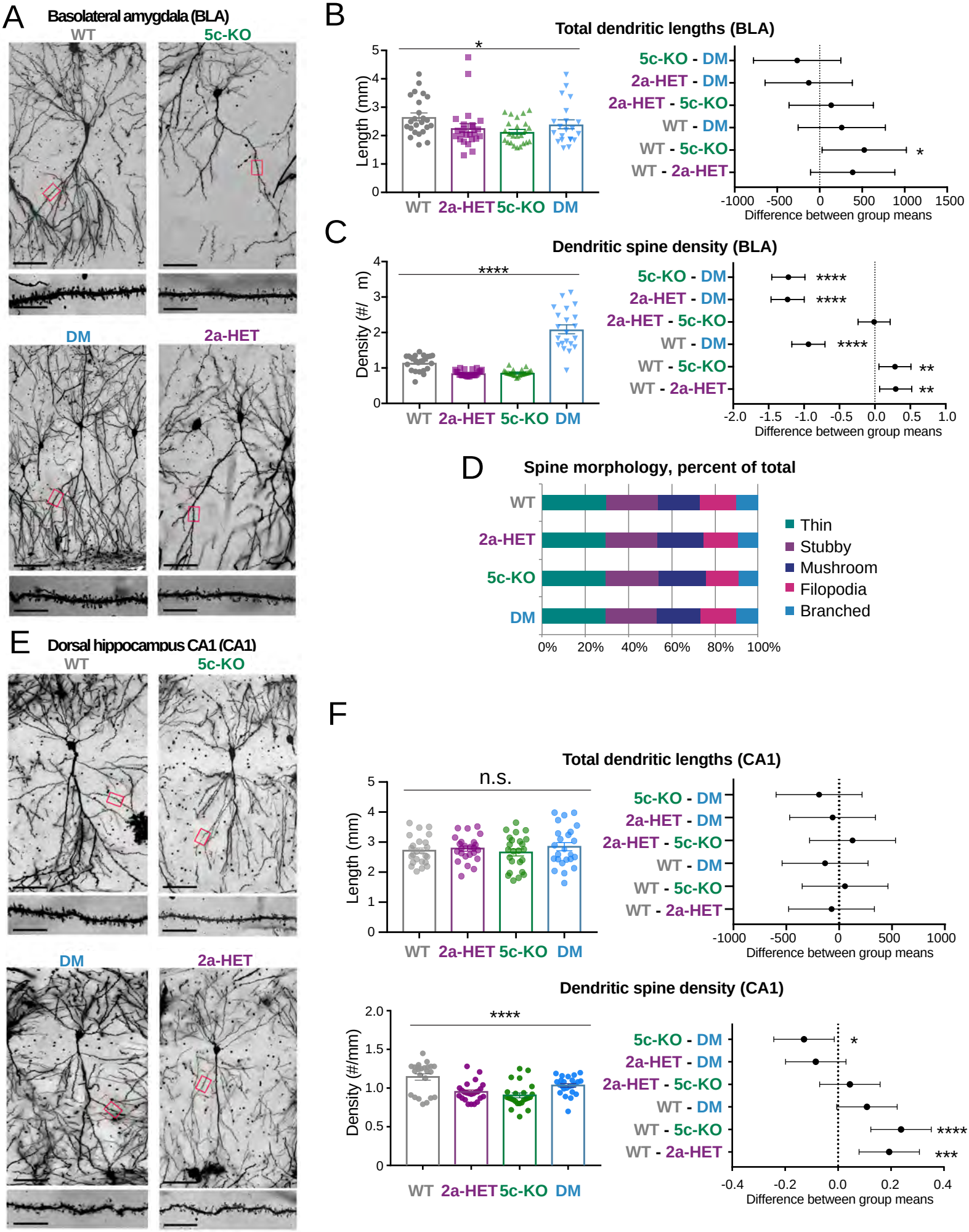
A
Basolateral amygdala (BLA)
WT
5c-KO
DM
2a-HET
B
Total dendritic lengths (BLA)
Length (mm)
WT 2a-HET 5c-KO DM
5c-KO - DM
2a-HET - DM
2a-HET - 5c-KO
WT - DM
WT - 5c-KO
WT - 2a-HET
Difference between group means
C
Dendritic spine density (BLA)
Density (#/ m)
D
Spine morphology, percent of total
Thin
Stubby
Mushroom
Filopodia
Branched
E
Dorsal hippocampus CA1 (CA1)
F
Total dendritic lengths (CA1)
n.s.
Dendritic spine density (CA1)
Density (#/mm)

Figure 4

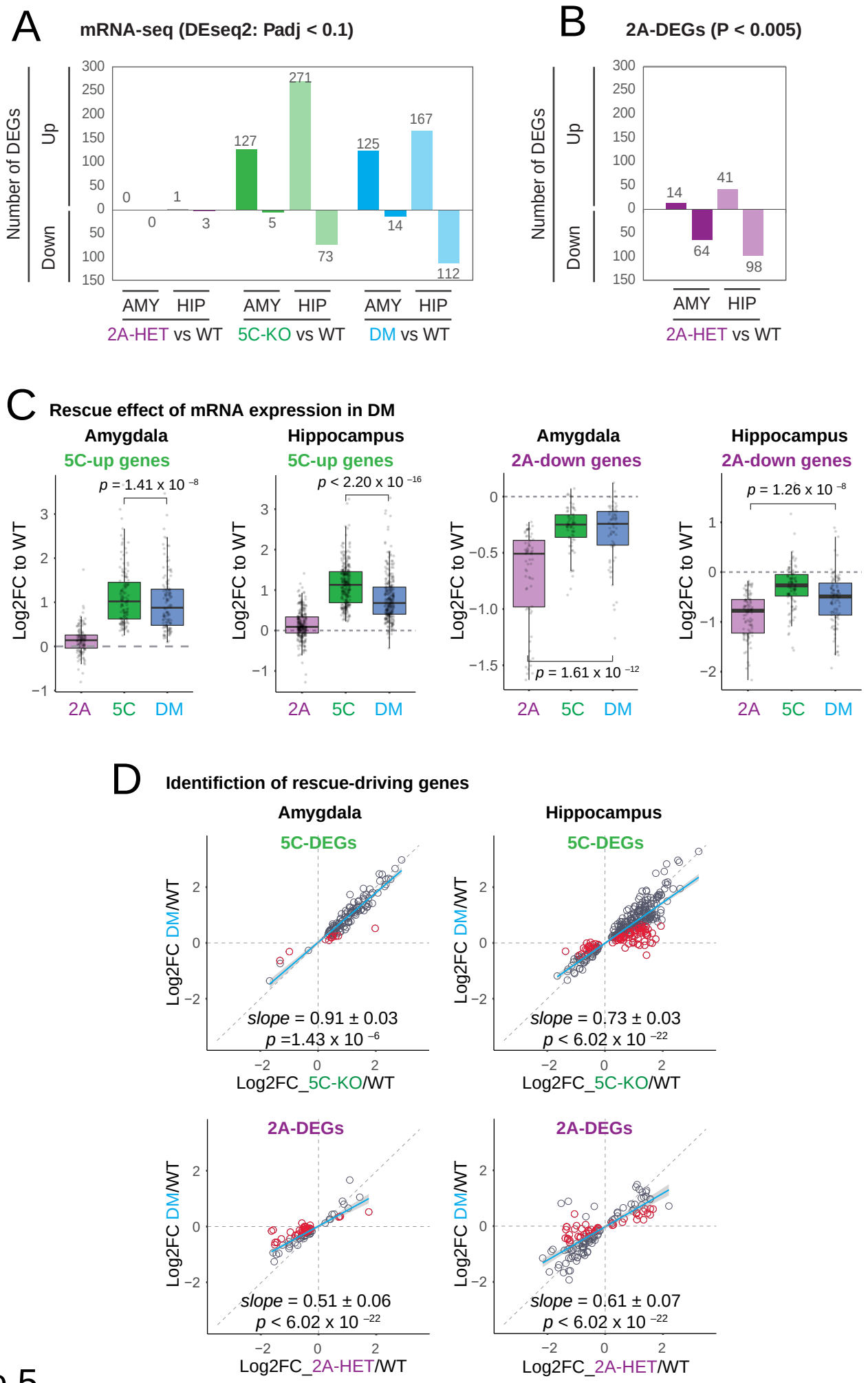
A
mRNA-seq (DEseq2: Padj < 0.1)
Number of DEGs
Up
Down
0
1
0
3
127
5
271
73
125
14
167
112
AMY
HIP
AMY
HIP
AMY
HIP
2A-HET vs WT
5C-KO vs WT
DM vs WT
B
2A-DEGs (P < 0.005)
14
64
41
98
AMY
HIP
2A-HET vs WT
C
Rescue effect of mRNA expression in DM
Amygdala
5C-up genes
p = 1.41 x 10 −8
Hippocampus
5C-up genes
p < 2.20 x 10 −16
Amygdala
2A-down genes
p = 1.61 x 10 −12
Hippocampus
2A-down genes
p = 1.26 x 10 −8
Log2FC to WT
2A
5C
DM
D
Identifiction of rescue-driving genes
Amygdala
Hippocampus
5C-DEGs
slope = 0.91 ± 0.03
p =1.43 x 10 −6
slope = 0.73 ± 0.03
p < 6.02 x 10 −22
2A-DEGs
slope = 0.51 ± 0.06
p < 6.02 x 10 −22
slope = 0.61 ± 0.07
p < 6.02 x 10 −22
Log2FC DM/WT
Log2FC_5C-KO/WT
Log2FC_2A-HET/WT

Figure 5

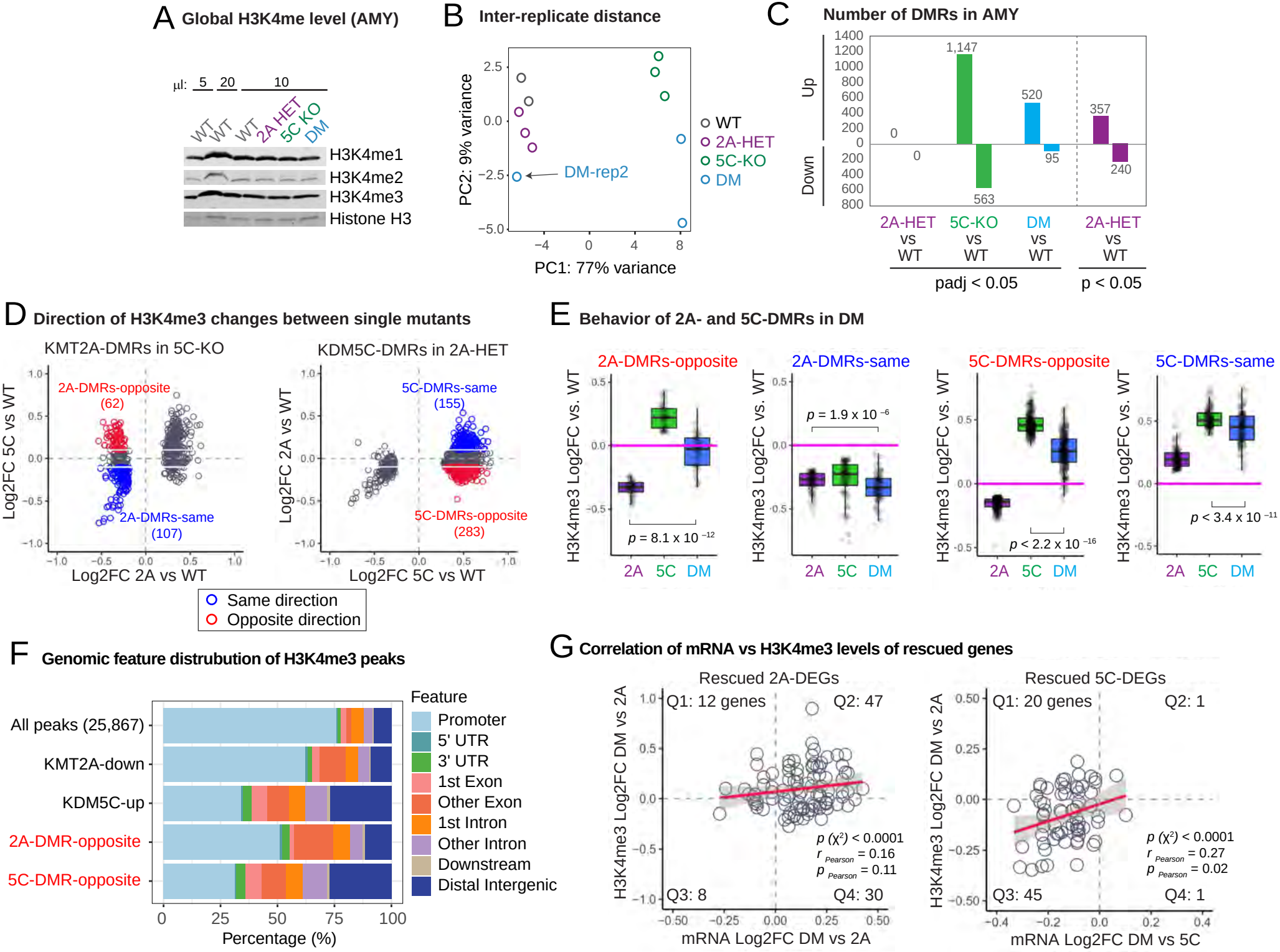
A Global H3K4me level (AMY)
µl: 5 20 10
WT WT WT 2A HET 5C KO DM
H3K4me1
H3K4me2
H3K4me3
Histone H3
B Inter-replicate distance
PC2: 9% variance
PC1: 77% variance
DM-rep2
WT
2A-HET
5C-KO
DM
C Number of DMRs in AMY
Up
Down
1,147
520
357
0
0
95
240
563
2A-HET vs WT
5C-KO vs WT
DM vs WT
2A-HET vs WT
padj < 0.05
p < 0.05
D Direction of H3K4me3 changes between single mutants
KMT2A-DMRs in 5C-KO
KDM5C-DMRs in 2A-HET
2A-DMRs-opposite (62)
2A-DMRs-same (107)
5C-DMRs-same (155)
5C-DMRs-opposite (283)
Log2FC 5C vs WT
Log2FC 2A vs WT
Log2FC 2A vs WT
Log2FC 5C vs WT
Same direction
Opposite direction
E Behavior of 2A- and 5C-DMRs in DM
2A-DMRs-opposite
2A-DMRs-same
5C-DMRs-opposite
5C-DMRs-same
H3K4me3 Log2FC vs. WT
p = 8.1 x 10 −12
p = 1.9 x 10 −6
p < 2.2 x 10 −16
p < 3.4 x 10 −11
2A 5C DM
F Genomic feature distrubution of H3K4me3 peaks
All peaks (25,867)
KMT2A-down
KDM5C-up
2A-DMR-opposite
5C-DMR-opposite
Percentage (%)
Feature
Promoter
5' UTR
3' UTR
1st Exon
Other Exon
1st Intron
Other Intron
Downstream
Distal Intergenic
G Correlation of mRNA vs H3K4me3 levels of rescued genes
Rescued 2A-DEGs
Rescued 5C-DEGs
Q1: 12 genes
Q2: 47
Q3: 8
Q4: 30
Q1: 20 genes
Q2: 1
Q3: 45
Q4: 1
p (χ²) < 0.0001
r Pearson = 0.16
p Pearson = 0.11
p (χ²) < 0.0001
r Pearson = 0.27
p Pearson = 0.02
H3K4me3 Log2FC DM vs 2A
mRNA Log2FC DM vs 2A
mRNA Log2FC DM vs 5C

Figure 6

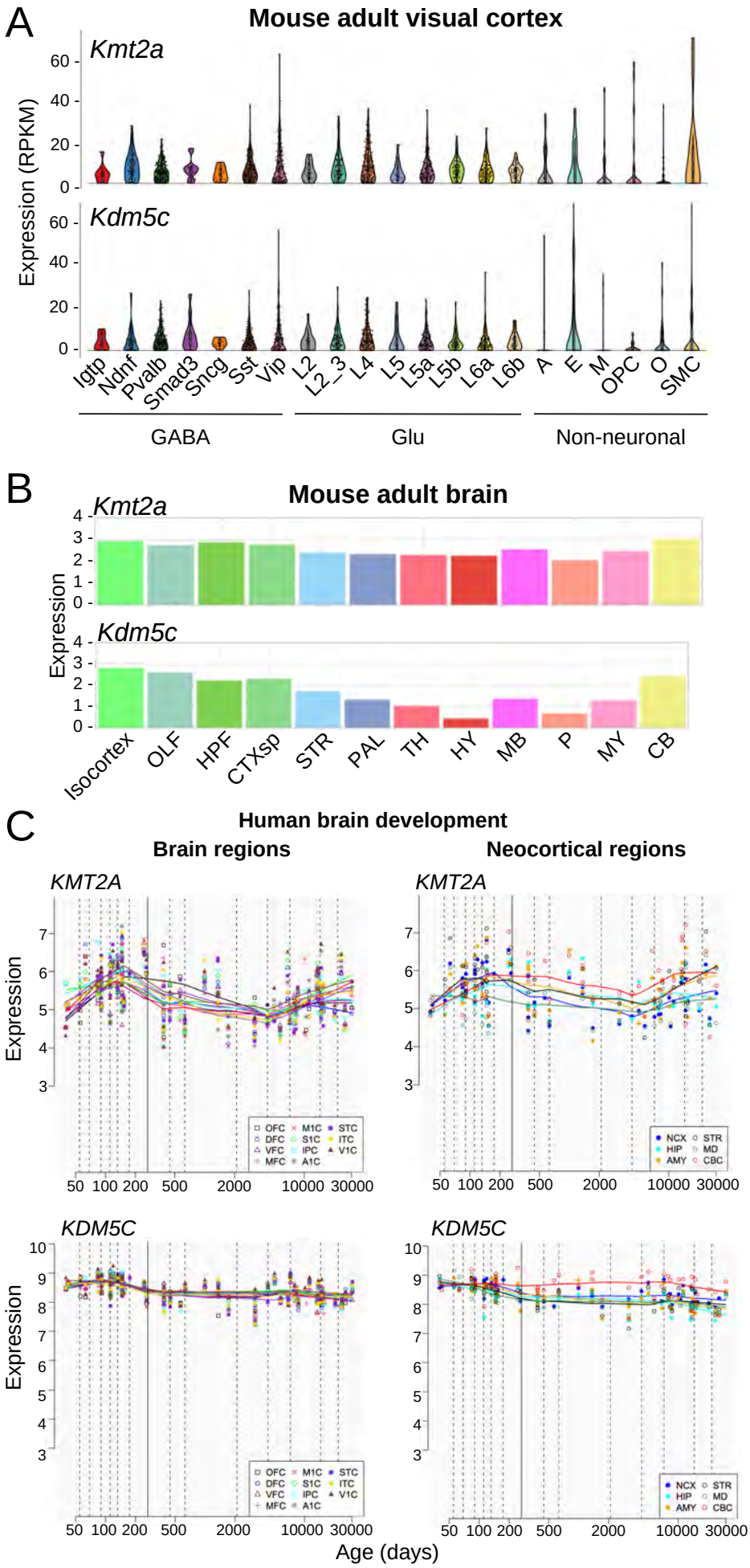

Supplementary Figure 1

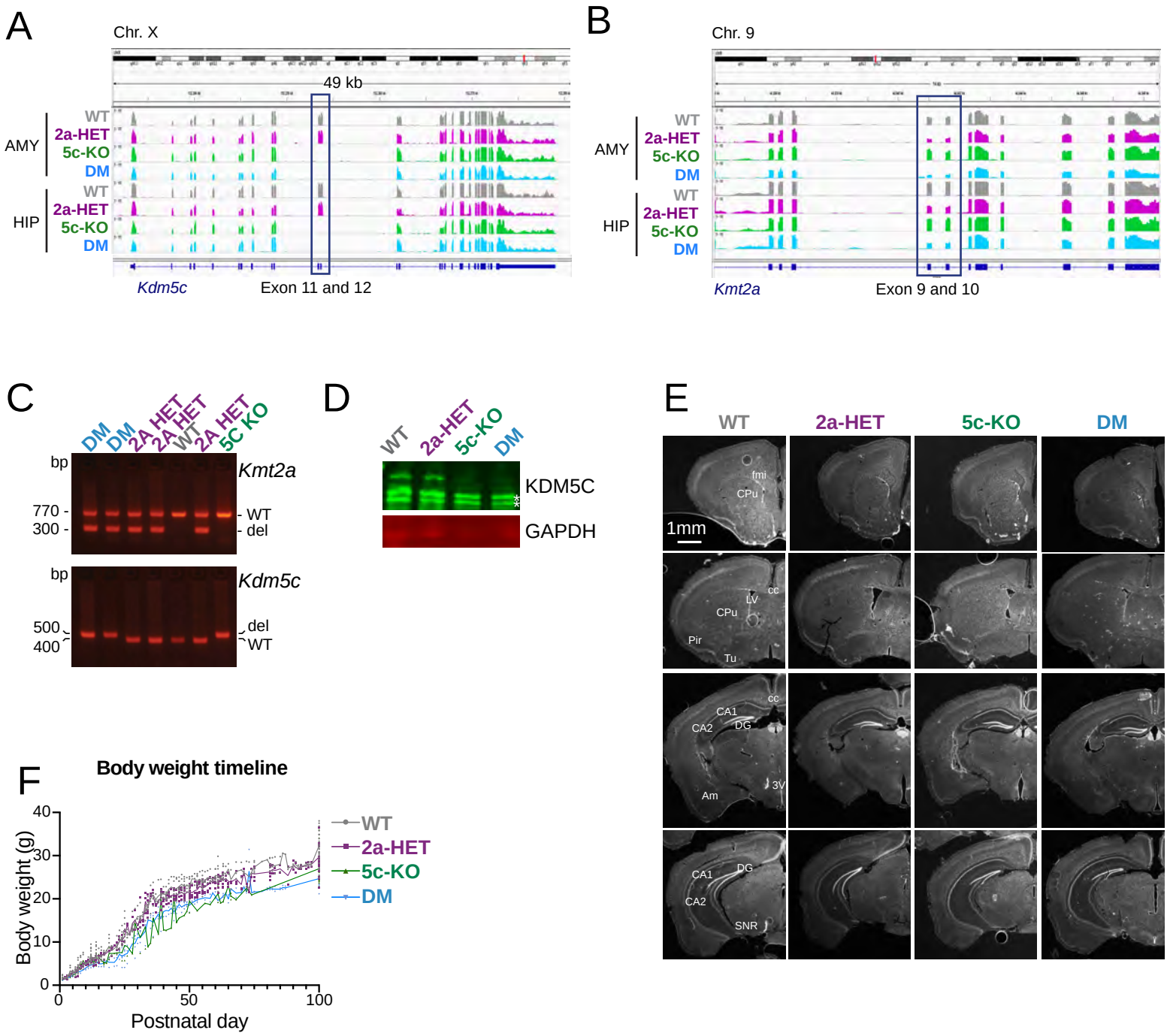

Supplementary Figure 2

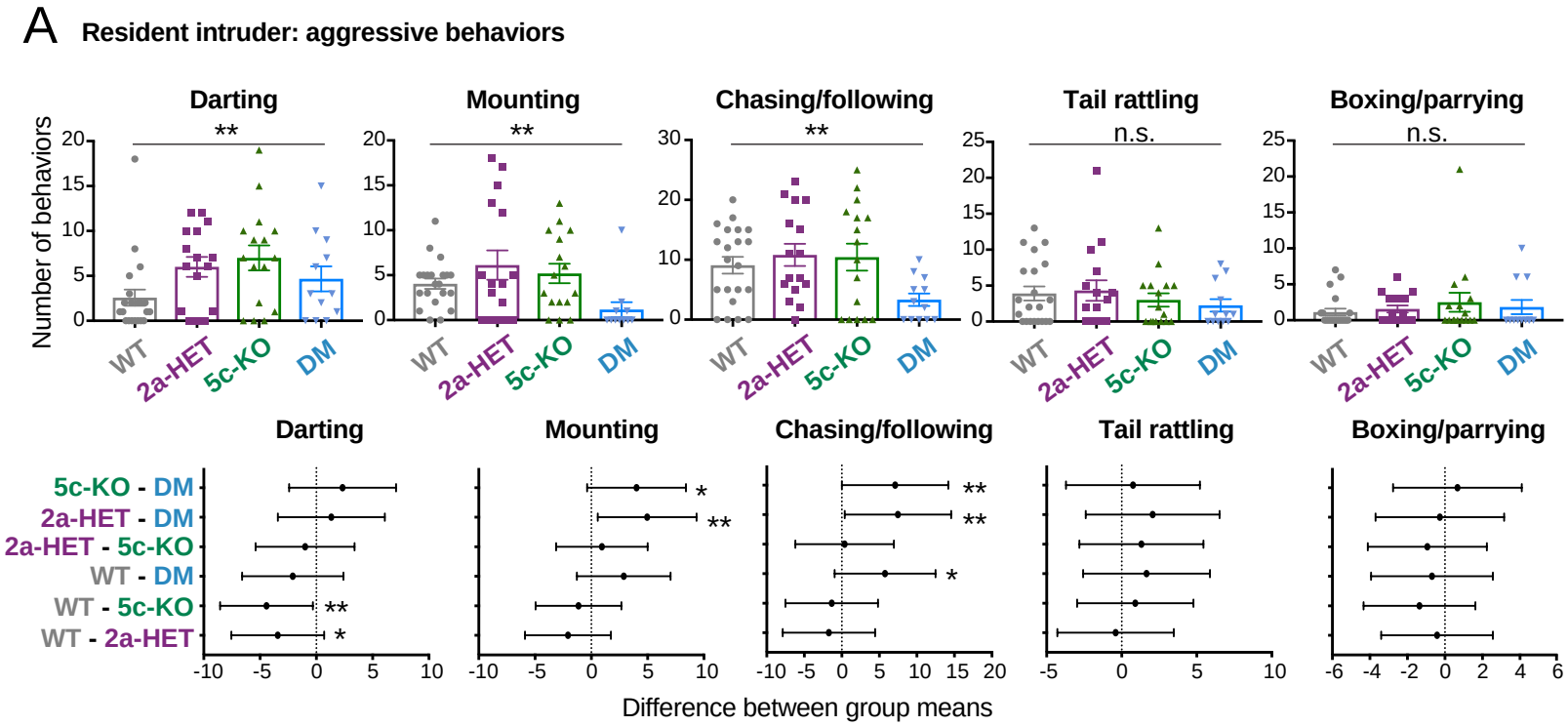

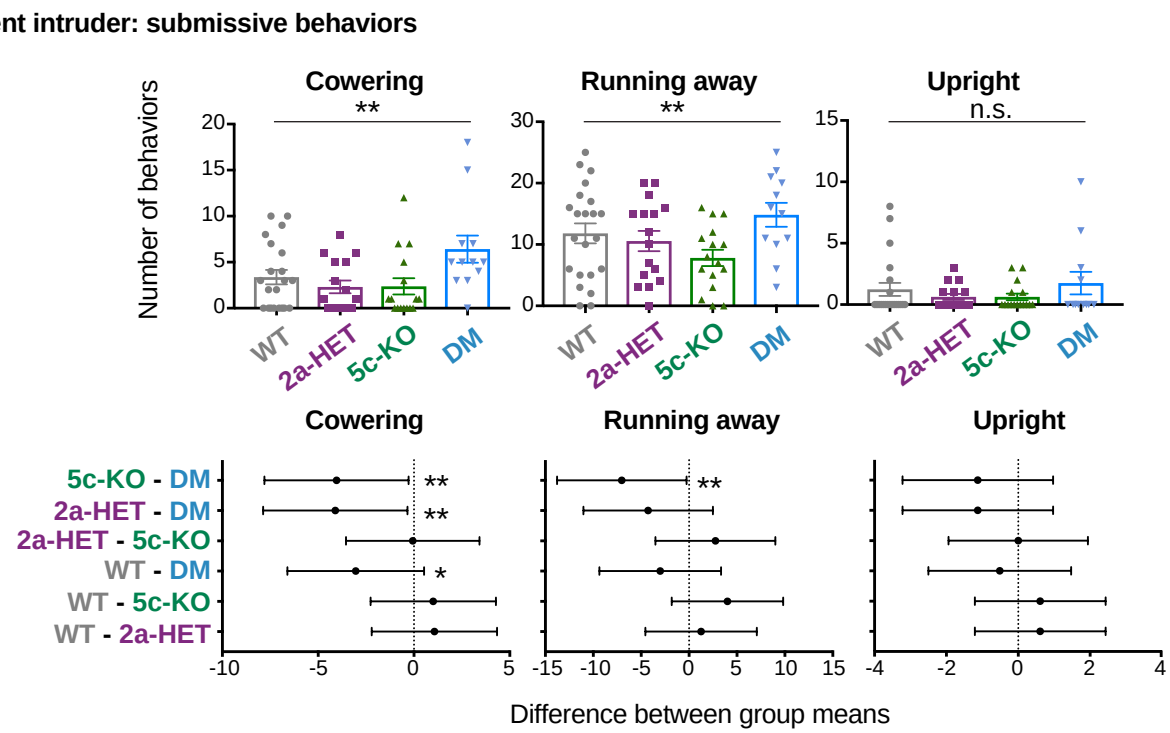

Supplementary Figure 3

A

Dendritic spine subtypes

1. Filopodia
2. Thin
3. Stubby
4. Mushroom
5. Branched

Supplementary Figure 4

A **Euclidean distances between RNA-seq samples from various brain regions**

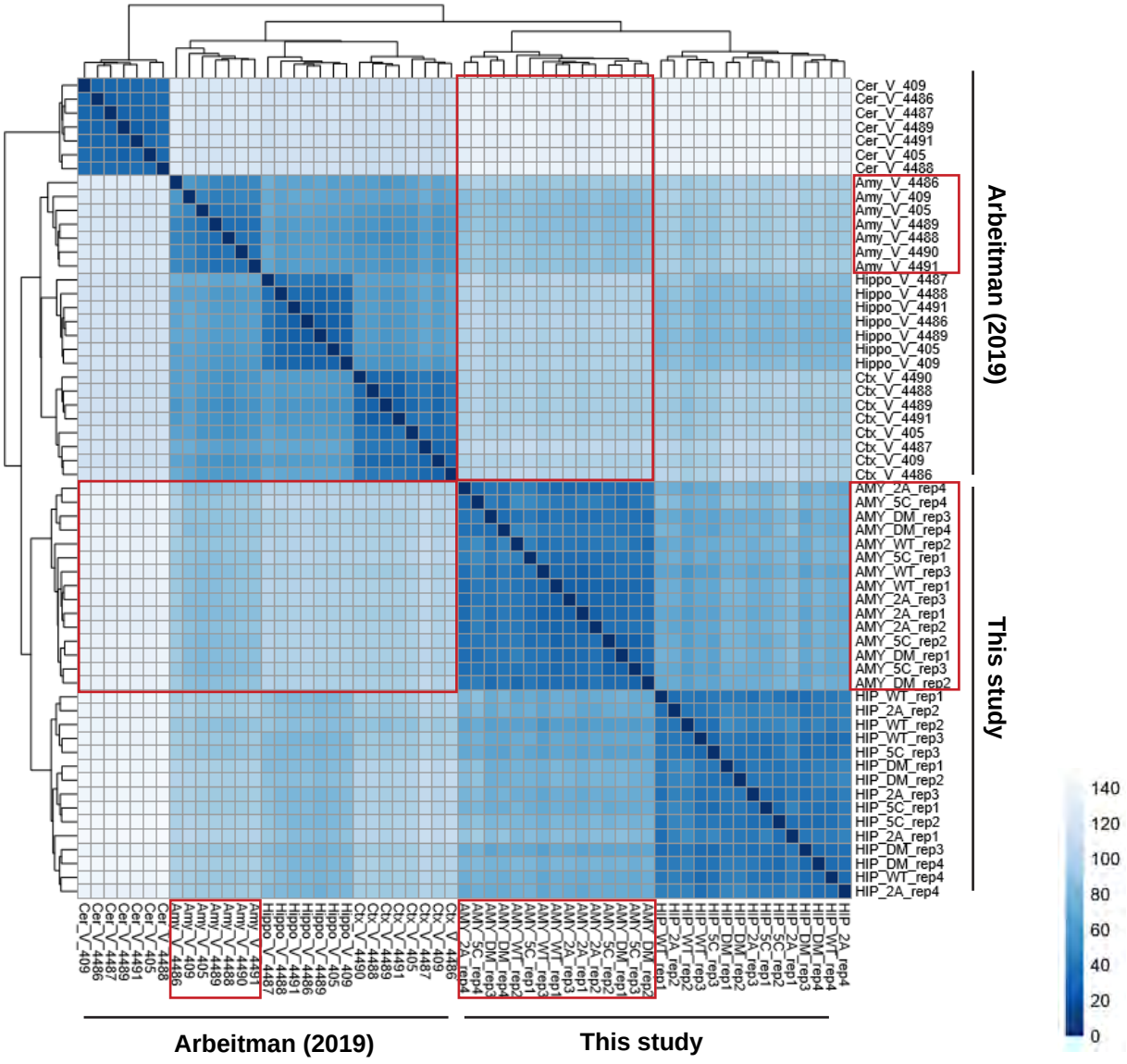

Supplementary Figure 5

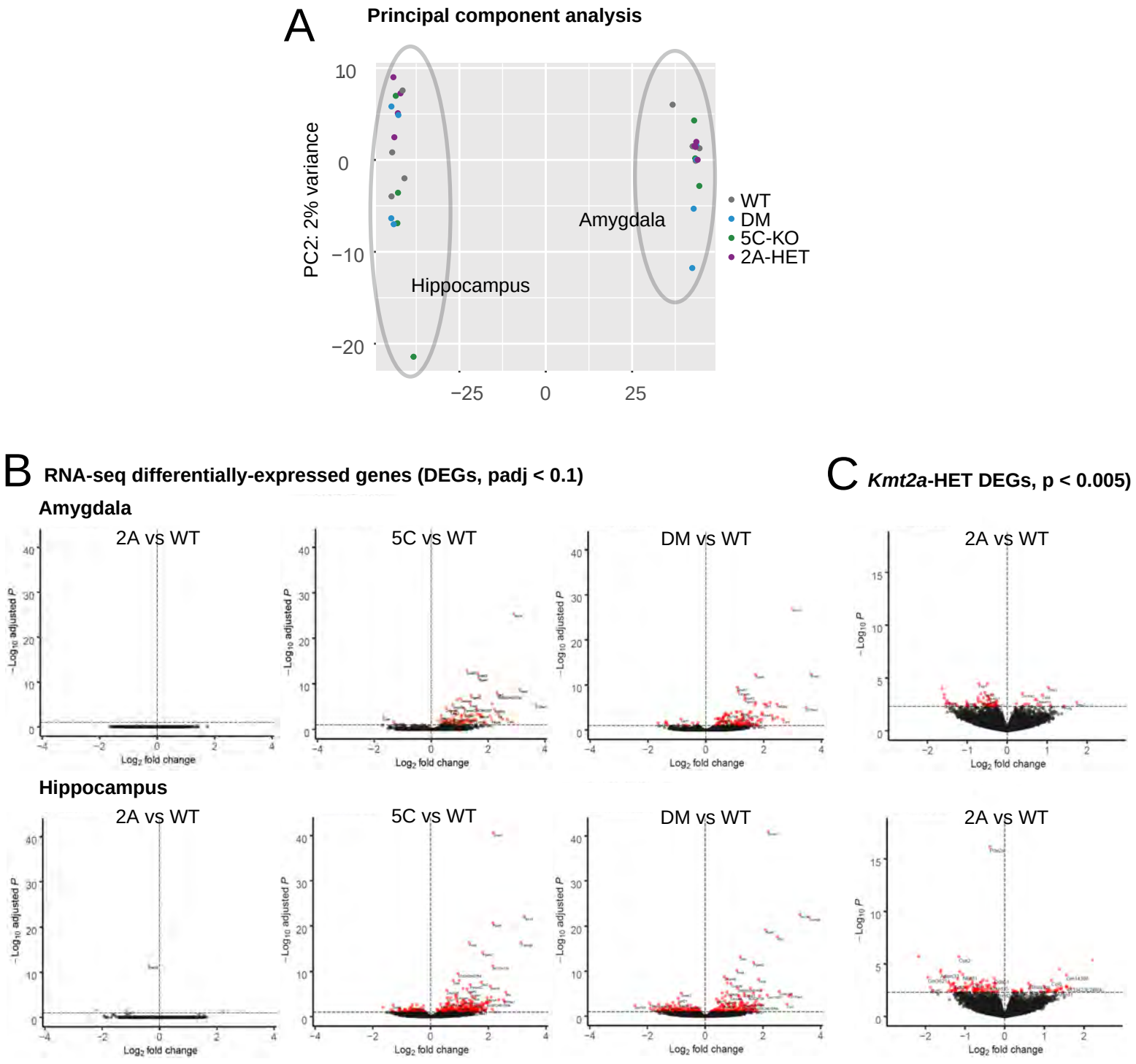

Supplementary Figure 6

A **Overlap DEGs between tissues**

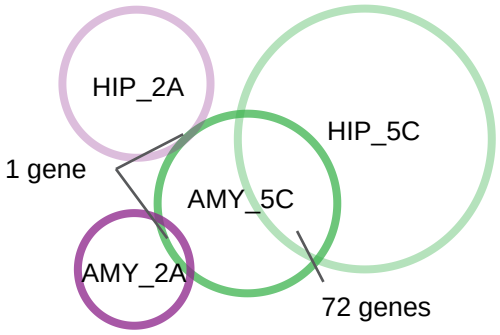

B **Similarity in DEG expression between the two brain regions**

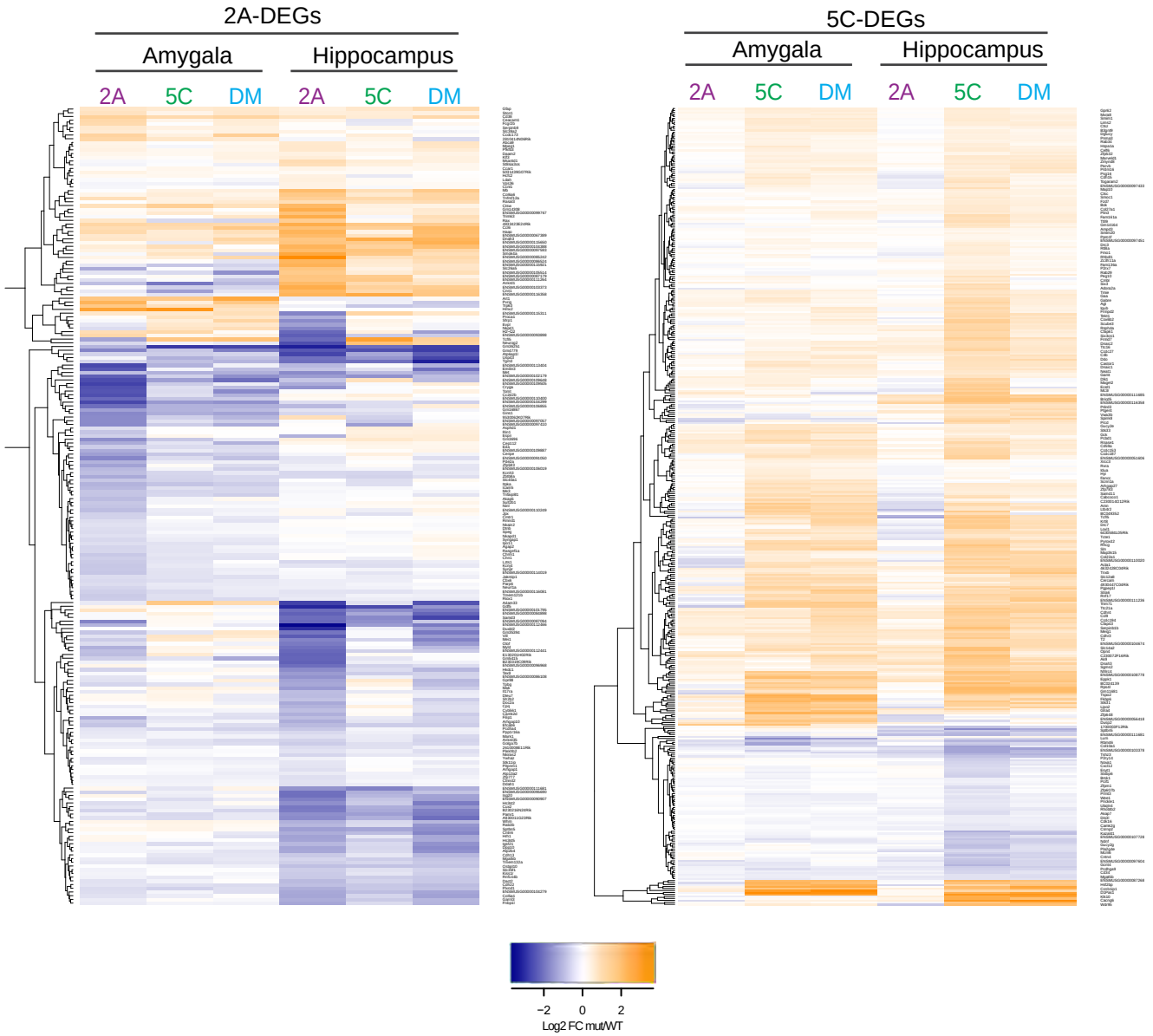

Supplementary Figure 7

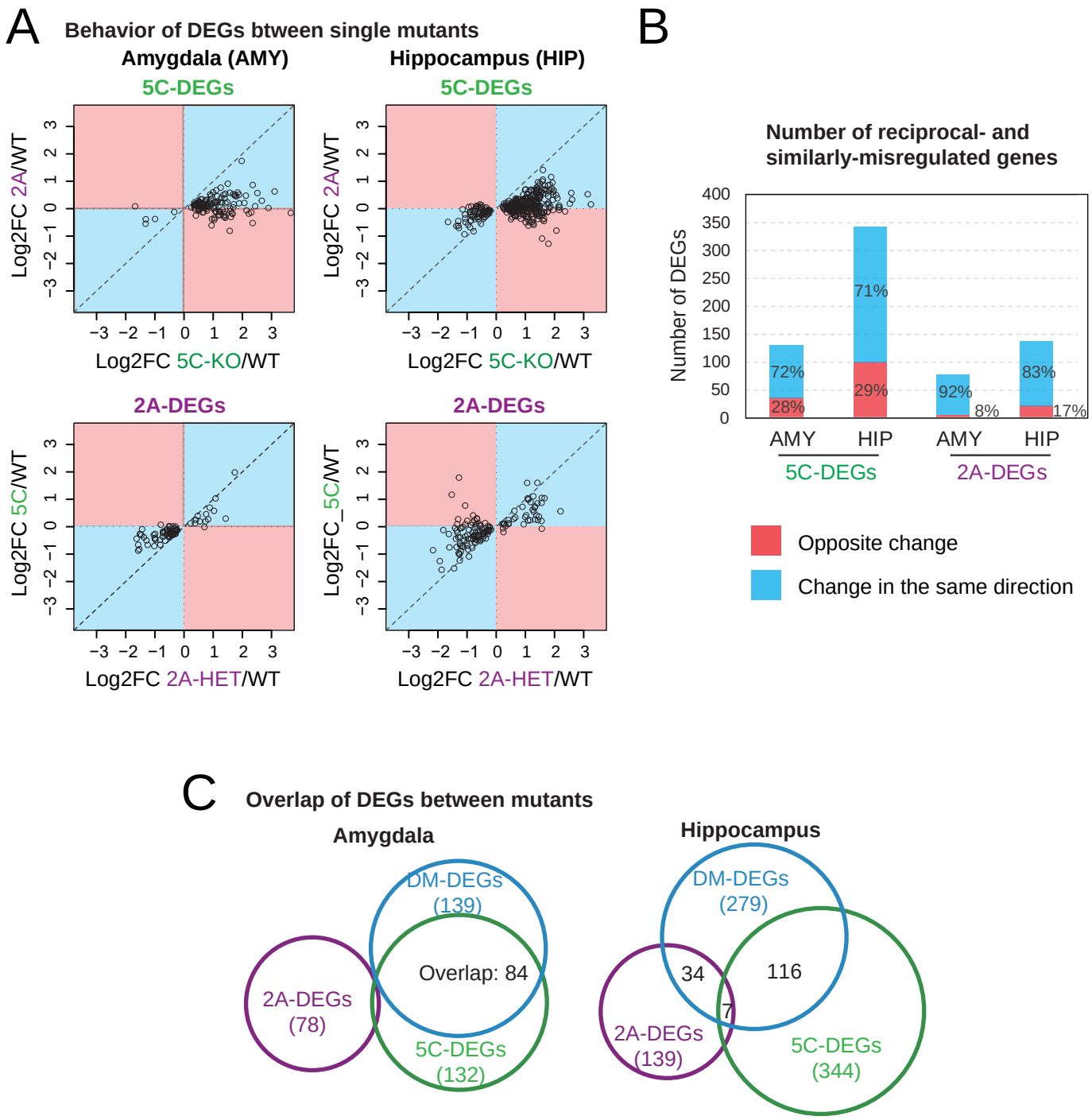

Supplementary Figure 8

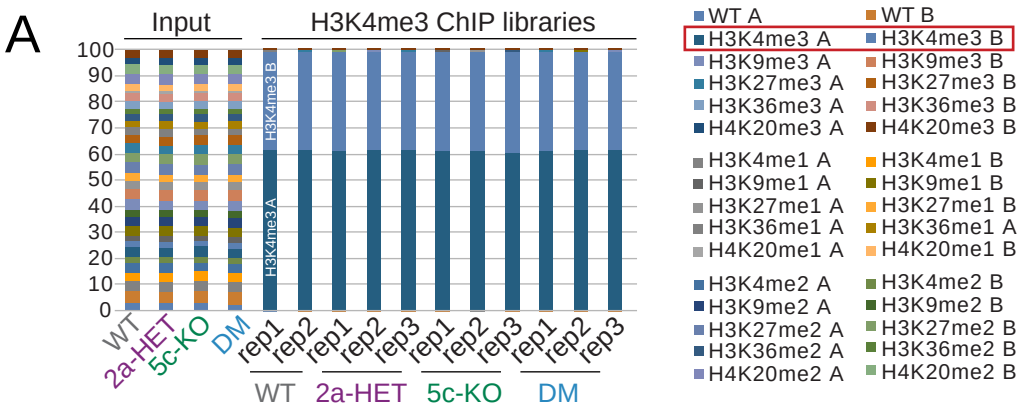

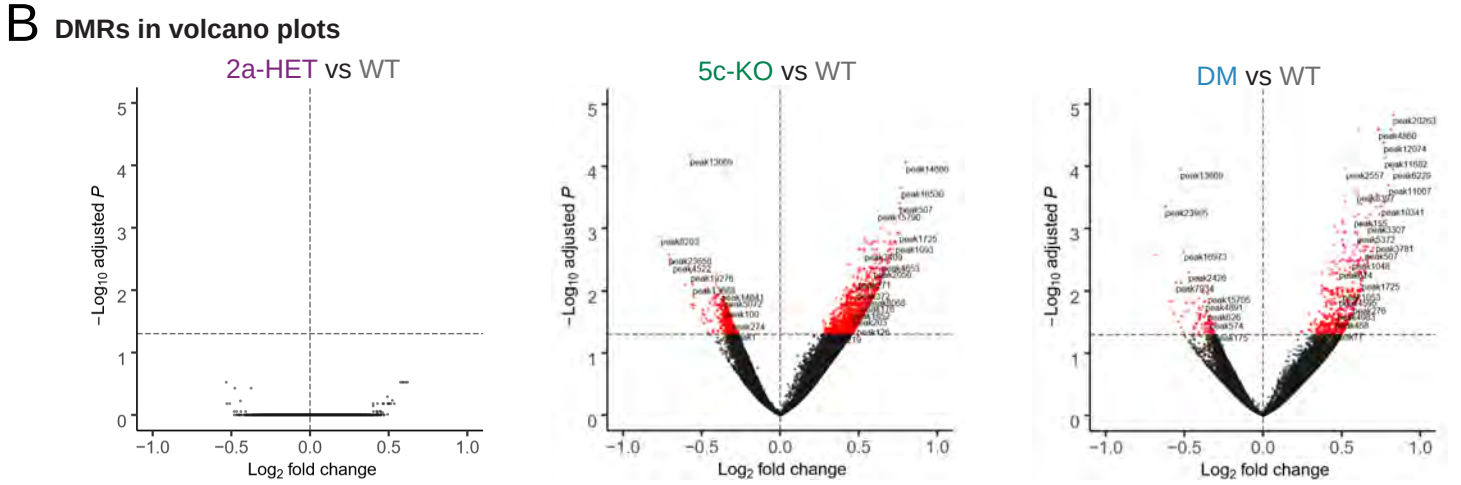

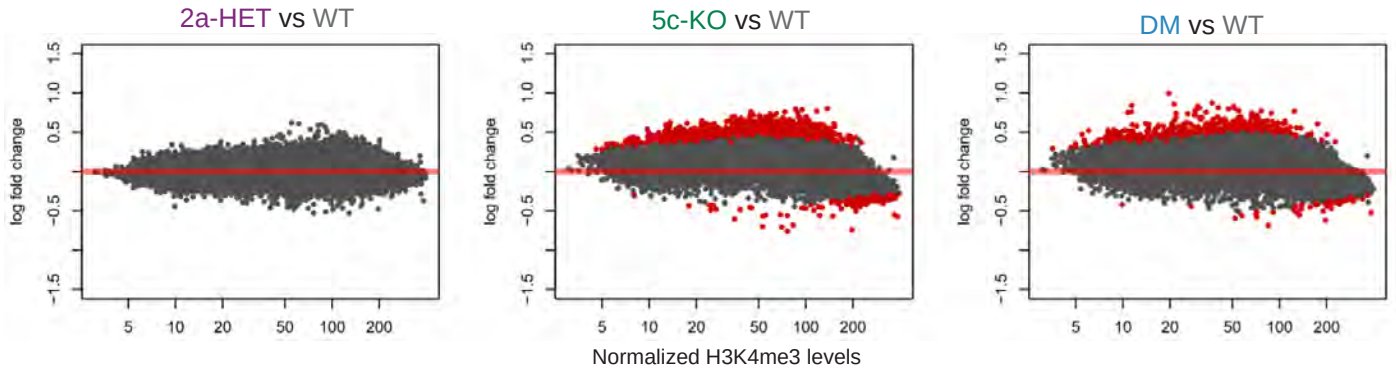

Supplementary Figure 9

A **Behavior of 2A- and 5C-DMRs in DM without DM-rep2**

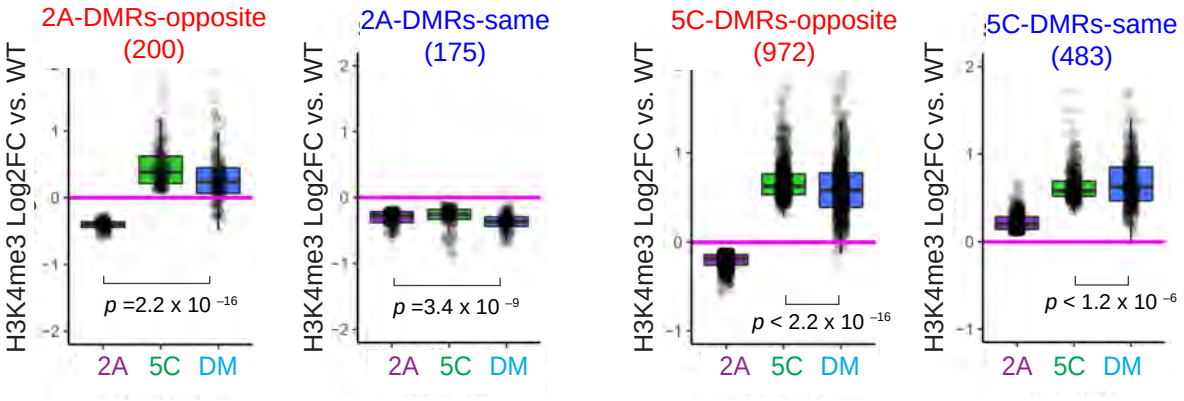

Supplementary Figure 10

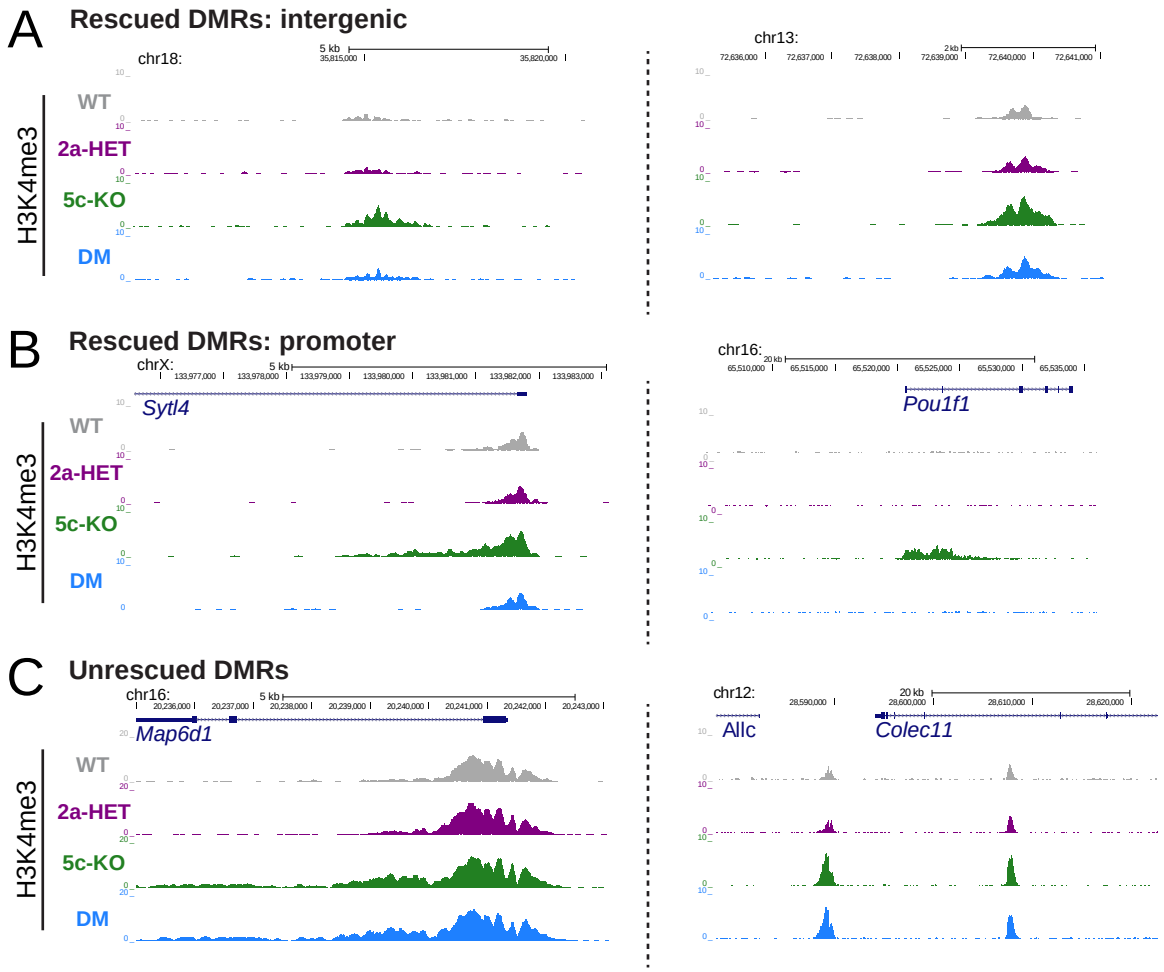

Supplementary Figure 11